REPUBLIC OF TURKEY
YILDIZ TECHNICAL UNIVERSITY
GRADUATE SCHOOL OF SCIENCE AND ENGINEERING

NUMERICAL STUDY OF THE DOUBLE MACH REFLECTION USING SHOCK-CAPTURING WITH SUB-CELL ACCURACY

BURCU ÇİZME

MSc. THESIS
DEPARTMENT OF MECHANICAL ENGINEERING
PROGRAM OF HEAT AND PROCESSING

ADVISER
PROF. DR. HAKAN DEMİR

İSTANBUL, 2019

REPUBLIC OF TURKEY

YILDIZ TECHNICAL UNIVERSITY

GRADUATE SCHOOL OF SCIENCE AND ENGINEERING

NUMERICAL STUDY OF THE DOUBLE MACH REFLECTION USING SHOCK-CAPTURING WITH SUB-CELL ACCURACY

A thesis submitted by Burcu ÇİZME in partial fulfillment of the requirements for the degree of **MASTER OF SCIENCE** is approved by the committee in 28.03.2019 in Department of Mechanical Engineering, Heat and Processing Program.

Thesis Adviser

Prof. Dr. Hakan DEMİR

Yıldız Technical University

Approved By the Examining Committee

Prof. Dr. Hakan DEMİR

Yıldız Technical University _____

Prof. Dr. Ali PINARBAŞI

Yıldız Technical University _____

Prof. Dr. Hasan A. HEPERKAN

İstanbul Aydın University _____

ACKNOWLEDGEMENTS

I would like to thank to my adviser, Prof. Dr. Hakan DEMİR, for supporting me for the purpose of completing my master studies. Besides my adviser, I would like to thank the rest of my thesis committee.

I would particularly like to single out my supervisor at Technical University of Darmstadt, M.Sc. Markus Geisenhofer. I am very grateful to him for his scientific advices, knowledge, many insightful discussions and suggestions. He was my primary resource for getting my science questions answered and was instrumental in helping me, all in eight months during my Erasmus semester in TU Darmstadt. I also thank my supervisors from TU Darmstadt, Prof. Dr.-Ing. Habil. Martin Oberlack, Dr.-Ing. Björn Müller and Dr.-Ing. Florian Kummer for their helps and leadings.

I would also like to thank my parents Şeniz Çizme and Ali Çizme, for supporting me spiritually throughout my life.

March, 2019

Burcu ÇİZME

TABLE OF CONTENTS

Page

LIST OF SYMBOLS vii

LIST OF ABBREVIATIONS viii

LIST OF FIGURES ix

LIST OF TABLES xii

ABSTRACT xiii

ÖZET xv

CHAPTER 1

INTRODUCTION 1

1.1 Literature Review 1
1.2 Objective of the Thesis 1
1.3 Hypothesis 2

CHAPTER 2

FUNDAMENTALS 3

2.1 Numerical Methods 3
2.2 Compressible Flow 4
2.2.1 Speed of Sound and Mach Number 6
2.2.1.1 Speed of Sound 6
2.2.1.2 Mach Number 8
2.2.2 Flow Regimes 8
2.2.2.1 Subsonic Flow 9
2.2.2.2 Transonic Flow 10
2.2.2.3 Supersonic Flow 10
2.2.2.4 Hypersonic Flow 11

CHAPTER 3

SHOCK WAVES AND SHOCK WAVE REFLECTIONS 12

3.1 Shock Waves 12

3.1.1 One-dimensional Phenomena: Normal Shock Waves 13
3.1.1.1 One-dimensional Flow Equations 14
3.1.1.2 Normal Shock Relations 16
3.1.2 Two-dimensional Phenomena: Oblique Shock Wave 17
3.1.2.1 Oblique Shock Relations 19
3.2 Shock Wave Reflections 22
3.2.1 Reasons for the Reflections 23
3.2.2 Analytical Approaches for Describing Regular and Mach Reflections 24
3.2.2.1 Two-Shock Theory (2ST) for an Inviscid Flow 26
3.2.2.2 Three-Shock Theory (3ST) for an Inviscid Flow 27
3.2.3 Modifications of the Perfect Inviscid Analytical Approaches 29
3.2.3.1 Nonstraight Discontinuities 29
3.2.3.2 Thermal Conduction Effects 30
3.2.3.3 Real Gas Effects 30

CHAPTER 4

DOUBLE MACH REFLECTION 31

4.1 DMR Character 31
4.2 Analytical Solutions and Approaches 34

CHAPTER 5

SIMULATIONS 38

5.1 Summary of Reference Article 38
5.2 Steps of this Study 39
5.2.1 Compressible Navier-Stokes Files 39
5.2.2 High Performance Computing 40
5.2.3 Bounded Support Spectral Solver 40
5.2.4 VisIt 40
5.2.5 Engauge Digitizer 41
5.2.6 Summary of the Process 42
5.3 Introduction for Simulations 43
5.4 Problems of Simulations 44
5.4.1 Kink on Mach Stem 44
5.4.2 Recirculation in Area (3) 45
5.4.3 Irregularity on Incident Shock Wave from IBM Simulations 46
5.4.4 Trace of Incident Shock Wave 46
5.5 Comparison 48
5.5.1 Effect of Maximum Y Height 48
5.5.2 Grid Comparison 48
5.5.2.1 Coarsest and Finest Grid Cells 49
5.5.2.2 All 0^{th} DG Degrees: For Boundary Fitted Method for 0.25 End Time with 0^{th} DG Degree 51
5.5.3 Degree Comparison 51
5.5.3.1 Coarsest and Finest Grid Cells 51
5.5.3.2 0^{th}, 1^{st} and 2^{nd} DG degrees at 0.25 End Time 52
5.5.3.3 1^{st} and 3^{rd} DG degrees at 0.20 End Time 53
5.5.4 Immersed Boundary – Boundary Fitted Methods 53
5.5.5 End Time Comparison 54

5.5.6 Article Comparison 54
5.6 Analytical Solutions 55

CHAPTER 6

RESULTS AND DISCUSSION 63

REFERENCES 65

APPENDIX-A

COMPRESSIBLE NAVIER-STOKES SOLVER 66

CURRICULUM VITAE 71

LIST OF SYMBOLS

τ	Compressibility
ν	Volume
p	Pressure
ρ	Density
a	Speed of sound
V	Local velocity in flow
γ	Specific heat capacities ratio
C_p	Specific heat capacity at constant pressure
C_v	Specific heat capacity at constant volume
M_0	Mach Number
h	Enthalpy
t	Time
i	Incident Shock Wave
r	Reflected Shock Wave
m	Mach Stem
s	Slip Line
r'	Secondary Reflected Shock Wave
m′	Secondary Mach Stem
s'	Secondary Slip Line
R	Reflection Point
K	Kink Point
T	Temperature
T'	First Triple Point
T"	Second Triple Point
Φ	Flow's Angle
θ_w	Wedge Angle

LIST OF ABBREVIATIONS

2ST	Two-Shock Theory
3ST	Three-Shock Theory
BFM	Boundary Fitted Method
BoSSS	Bounded Support Spectral Solver
CMR	Complex Mach Reflection
CNS	Compressible Navier-Stokes
DG	Discontinuous Galerkin
DiMR	Direct Mach Reflection
DMR	Double Mach Reflection
FEM	Finite Element Method
FVM	Finite Volume Method
HPC	High Performance Computing
IBM	Immersed Boundary Method
InMR	Inverse Mach Reflection
IR	Irregular Reflection
MR	Mach Reflection
PTMR	Pseudo-Transitional Mach Reflection
RR	Regular Reflection
SMR	Single Mach Reflection
StMR	Stationary Mach Reflection
TMR	Transitional Mach Reflection
TRR	Transitioned Regular Reflection

LIST OF FIGURES

Page

Figure 2.1 (a) Finite Volume (FVM) for 0^{th} DG degree, (b) Finite Element (FEM) for 1^{st} DG degree and (c) Discontinuous Galerkin for 1^{st} DG degree [4] 3
Figure 2.2 Boundary Fitted Method 4
Figure 2.3 Compressible flow simulation, computed with Immersed Boundary Method (IBM) [7] 4
Figure 2.4 Schematic of a sound wave, based on [2] 7
Figure 2.5 Illustration of different regimes of flow [2] 9
Figure 3.1 Comparison between subsonic and supersonic streamlines for flow over a flat-faced cylinder or slab, based on [2] 12
Figure 3.2 Diagram of a normal shock, based on [8] 14
Figure 3.3 Rectangular control volume for one-dimensional flow, based on [2] 15
Figure 3.4 Supersonic flow over a corner [2] 18
Figure 3.5 The propagation of disturbances in (a) subsonic and (b) supersonic flow [2] 18
Figure 3.6 Comparison between the wave angle and the Mach angle [2] 19
Figure 3.7 Oblique shock wave geometry [2] 19
Figure 3.8 Weak and strong shocks [2] 21
Figure 3.9 Attached and detached shocks [2] 21
Figure 3.10 θ-β-M curves. Oblique shock properties [2] 22
Figure 3.11 The 13 possible shock wave reflection configurations [9] 23
Figure 3.12 Flow over a wedge in a steady flow: (a) $M_0 < 1$, smooth subsonic turning; (b) $M_0 > 1$ and $\theta_w < \theta_{max}(M_0)$, straight and attached oblique shock wave; (c) $M_0 > 1$ and $\theta_w > \theta_{max}(M_0)$, detached bow shock wave [9] 24
Figure 3.13 Definition of parameters across an oblique shock wave [9] 25
Figure 3.14 Schematic illustration of the wave configuration of a RR [9] 26
Figure 3.15 Schematic illustration of the wave configuration of an MR [9] 27
Figure 4.1 Four different shock wave reflections, (a) Regular Reflection (RR), (b) Single Mach Reflection (SMR), (c) Complex Mach Reflection (CMR) and (d) Double Mach Reflection (DMR) [3] 31
Figure 4.2 Domains of different oblique shock wave diffractions in $(Ms, \theta w)$ plane [3] 32
Figure 4.3 Double Mach reflection general characteristic, based on [3] 34
Figure 4.4 DMR characteristic for Ben-Dor approach, based on [9] 35
Figure 4.5 DMR characteristic for Law-Glass approach (a) simplified schema and (b) Law Glass DMR schema [10] 36
Figure 5.1 Density curves from reference article; (a) density curves and (b) zooming at the results [1] 39
Figure 5.2 Special mesh which the reference article used 39

Figure 5.3 BoSSS [7] 40
Figure 5.4 VisIt examples for plot options with ρ values for simulation 800x280 grid cells at 0.20 end time for 3rd DG degree: (a) Pseudocolor, (b) Contour, (c) Curve 41
Figure 5.5 Process which is generally followed to reach the results 42
Figure 5.6 Several simulations which were resolved: (a) Finest grid cells for 0.20 end time, (b) Finest grid cells for 3rd DG degree, (c) Finest grid cells among IBM simulations 44
Figure 5.7 The Kink which appears on Mach stem on the simulation 800x200 grid cells at 0.25 end time for 0th DG degree, values for (a) Density, (b) Pressure 44
Figure 5.8 Detailed plot from the area (3) for 800x280 at 0.20 end time and 3rd DG degree, values for (a) Density, (b) Pressure 45
Figure 5.9 Recirculation (a) between area (4)-(5) and (b) recirculation in area (3) ... 45
Figure 5.10 Irregularity on incident shock wave (a) 600x420 grid cells at 0.25 end time for 0th DG degree (IBM) and (b) 600x525 grid cells at 0.25 end time for 0th DG degree (IBM) 46
Figure 5.11 Fluctuations on incident shock wave on simulation 800x280 grid cells at 0.20 end time for 3rd DG degree (a) for density and (b) for pressure 47
Figure 5.12 Fluctuations on incident shock wave at half time steps on simulations (a) 800x280 grid cells at 0.20 end time for 3rd DG degree and (b) 1024x1024 grid cells at 0.20 end time for 0th DG Degree (IBM) for pressure 47
Figure 5.13 Effect of maximum Y height for 400x100 grid cells at 0.25 end time for 3rd DG Degree and 400x140 grid cells at 0.25 end time for 3rd DG degree ... 48
Figure 5.14 The coarsest and the finest grid cells for 0th DG degree, (a) 800x200 grid cells at 0.25 end time for 0th DG degree, (b) 2400x600 grid cells at 0.25 end time for 0th DG degree 49
Figure 5.15 The coarsest and the finest grid cells comparison for BFM, 0.25 end time with 0th DG degree 50
Figure 5.16 The coarsest and the finest grid cells for 0th DG degree (IBM) 50
Figure 5.17 All BFM at 0.25 end times for 0th DG degrees 51
Figure 5.18 3rd DG degrees and finest grid cells comparison with curves 52
Figure 5.19 0th, 1st and 2nd DG degrees comparison with curves 52
Figure 5.20 1st and 3rd DG degrees at 0.20 end time comparison with curves 53
Figure 5.21 Immersed boundary and boundary fitted method comparison with curves 53
Figure 5.22 End time comparison with pseudocolor for (a) 800x200 grid cells at 0.25 end time for 1st DG degree and (b) 800x280 grid cells at 0.20 end time for 1st DG degree 54
Figure 5.23 Article comparison with curves 55
Figure 5.24 Area separation with ρ,p and u values 56
Figure 5.25 All angles and areas for calculations 57
Figure 5.26 Areas and angles on IBM simulation 58
Figure A.1 First part of the CNS file of the simulation 800x200 grid cells at 0.20 end time for 3rd DG degree 66
Figure A.2 Second part of the CNS file of the simulation 800x200 grid cells at 0.20 end time for 3rd DG degree 67
Figure A.3 Third part of the CNS file of the simulation 800x200 grid cells at 0.20 end time for 3rd DG degree 68

Figure A.4 Fourth part of the CNS file of the simulation 800x200 grid cells at 0.20 end time for 3rd DG degree 69
Figure A.5 Fifth part of the CNS file of the simulation 800x200 grid cells at 0.20 end time for 3rd DG degree 69

LIST OF TABLES

Page

Table 5.1 Convergence rate of entropy for adaptive mesh [1] …….……38
Table 5.2 BFM Simulations……...43
Table 5.3 IBM Simulations……44

ABSTRACT

NUMERICAL STUDY OF THE DOUBLE MACH REFLECTION USING SHOCK-CAPTURING WITH SUB-CELL ACCURACY

Burcu ÇİZME

Department of Mechanical Engineering

MSc. Thesis

Adviser: Prof. Dr. Hakan DEMİR

This thesis deals with the numerical and analytical studies of the Double Mach reflection (DMR). Double Mach reflection can occur when a shock wave encounters an obstacle. There are some unknowns when DMR is concerned. This thesis helps to make these unknowns solvable.

Compressible Navier-Stokes solver (CNS) is used for performing simulations. The simulations are based on immersed boundary method (IBM) and boundary fitted method (BFM).

This thesis consists of two main parts, fundamentals and numerical/analytical solutions. Firstly, literature research on fundamentals of numerical methods, shock waves and compressible flows are described. Secondly, numerical simulations of Double Mach reflection are performed on high-performance computing (HPC) system. While simulations are performed, the problems which are encountered, are explained and illuminated in detail. Simulations are compared with each other and also with the reference article [1]. In addition, simulations are analytically verified by equations from literatures.

Double Mach reflection studies are mostly experimental heretofore. Hence, in this study verification of simulations by determining the location of the first and second triple points T' and T'', respectively, which are the two breaking points of the Double Mach reflection, are done newly.

With literature research it is understood that without aid of simulations, the equations cannot be solved. For this reason, solving the equations using only initial conditions is terminated with failure. As a result, the values obtained from the simulations are applied to the equations and results are verified with small errors.

Key words: Shock wave, reflection, simulation, boundary fitted method, immersed boundary method

ÖZET

HÜCRE AYARLAMALARI İLE ŞOK YAKALAMA KULLANILARAK ÇİFT YANSIMANIN SAYISAL ÇALIŞMASI

Burcu ÇİZME

Makine Mühendisliği Anabilim Dalı

Yüksek Lisans Tezi

Tez Danışmanı: Prof. Dr. Hakan DEMİR

Bu tez, Çift Mach Yansıması'nın (DMR) nümerik ve analitik çalışmaları ile alakalıdır. Bir şok dalgası, herhangi bir engel ile karşılaştığında, Çift Mach Yansıması'nın oluşma imkanı vardır. DMR oluştuğunda bazı bilinmeyen parametreler söz konusudur. Bu tez, bahsedilen bilinmeyen parametrelerin çözülebilir olması için yardım niteliği taşımaktadır.

Sıkıştırılabilir Navier-Stokes çözücü (CNS), DMR simülasyonları için kullanılmıştır. Yürütülen simülasyonlar, temeli daldırılmış sınır metodu (IBM) ve sınıra uydurulmuş metod (BFM) olan ızgara yapıları kullanmaktadır.

Bu tez iki ana bölüm içermektedir; temeller ve nümerik/analitik çözümlemeler. İlk olarak, nümerik metotlar, şok dalgaları ve sıkıştırılabilir akış temelleri ile ilgili literatür incelemeleri yapılmıştır. İkinci olarak yüksek performanslı çözücüler (HPC) ile nümerik DMR analizleri gerçekleştirilmiştir. Simülasyonlar yürütülürken ortaya çıkan bazı problemler belirtilmiş ve detaylı olarak incelenmiştir. Simülasyonlardan elde edilen sonuçlar, kendi aralarında birbirleri ile ve referans makale [1] ile karşılaştırılmıştır. Ek olarak, simülasyonlar, literatürlerdeki denklemler ile analitik olarak doğrulanmıştır.

DMR çalışmaları şimdiye kadar çoğunlukla deneyseldir. Bundan dolayı bu tezde, DMR'nin iki kırılma noktası olan birincil ve ikincil üçlü noktanın, sırasıyla T' ve T'', yerlerinin belirlenmesi ile simülasyonların doğrulanması yeni olarak gerçekleştirilmiştir.

Literatür araştırmasında, sunulan denklemlerin, simülasyon yardımı olmadan analitik olarak çözülemeyeceği bilgisine ulaşılmıştır. Nitekim, sadece başlangıç koşulları ile denklemleri çözme girişimi başarısızlık ile sonuçlanmıştır. Bunların sonucu olarak, simülasyonlardan yeterli miktarda bazı değerler alınıp denklemlere eklenmiştir ve küçük hata oranları ile doğrulanmıştır.

Anahtar kelimeler: Şok dalgası, yansıma, simülasyon, sınıra uydurulmuş metot, daldırılmış sınır metodu

CHAPTER 1

INTRODUCTION

1.1 Literature View

Shock waves play an essential role in many technical fields including mechanical engineering, aerodynamics, physics and many more.

Shock wave formation is related with the Mach Number which is the value of speed of flow divided by speed of sound. Speed of gases are less than about 0.3 of the speed of sound [2]. Shock waves occur in flows which have Mach number values around and over 1.

At large, shock waves which have Mach numbers sufficiently high can be called strong waves. In this thesis, strong wave simulations which have Mach number 10 are performed.

This thesis consists of two main parts, fundamentals and numerical/analytical solutions. Firstly, literature research on fundamentals of numerical methods, shock waves and compressible flows are described. Secondly, numerical simulations of DMR are performed on high-performance computers. Compressible Navier-Stokes solver (CNS) is used for the simulations which have been performed. For simulations, two kind of meshes are used which are based on immersed boundary method (IBM) and boundary fitted method (BFM). BFM is more known than IBM and widely used.

The thesis will be completed by a short conclusions and outlook for following works.

1.2 Objective of the Thesis

Some kind of shock waves such as Double Mach Reflection (DMR) are very challenging to describe and are still not understood with their complete variety. Unlike other types of shock wave reflections, which have been studied well and analyzed both

experimentally and analytically in literatures, DMR studies are mostly experimental [3]. The possible reason for this situation could be the not sufficiently considered second triple point (*T*"), which DMR has. However, some analytical solutions are available and it is decided to study about DMR for the purpose of shoring up experimental results with analytical solutions. In addition, there are some formulas about the location of second triple point *T*" which, as far as known, have not been proved experimentally yet.

1.3 Hypothesis

The analytical solutions cannot be solved without numerical results. Due to this, simulations are analytically verified by equations from literatures.

While simulations are being performed, the problems are encountered and they are explained and illuminated in detail. Simulations are compared with each other and also with the reference article [1] for verifying.

CHAPTER 2

FUNDAMENTALS

First of all, fundamentals of numerical methods and compressible flow are described. The numerical methods will be essential for the later simulations. For understanding shock waves and DMR better, fundamentals of numerical methods and compressible flows should be understood well.

2.1 Numerical Methods

This section has characteristics of a short summary. Numerical methods which are necessary to know to resolve simulations are briefly noted. More detailed information can be obtained from references of Müller [4], [5].

Discontinuous Galerkin (DG) method, which can be seen as combination of the Finite Volume method (FVM) and the Finite Element method (FEM), is explained in Figure 2.1.

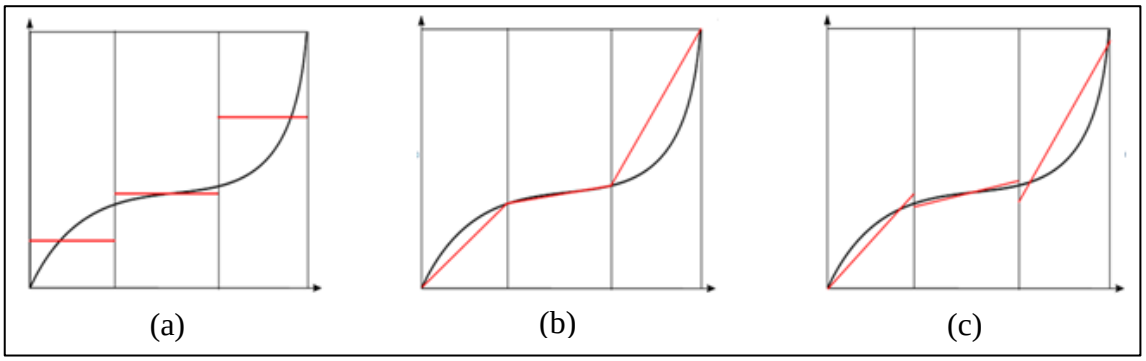


Figure 2.1 (a) Finite Volume (FVM) for 0^{th} DG degree, (b) Finite Element (FEM) for 1^{st} DG degree and (c) Discontinuous Galerkin (DG) for 1^{st} DG degree [4]

Immersed Boundary Method (IBM) is a numerical grid method that allows us to simulate boundaries in viscous flows and in the fluid grids which are not fitted to the

boundary shape. Unlike BFM, the fluid is modeled on a fixed cartesian mesh. The boundary moves freely through the fixed cartesian mesh.

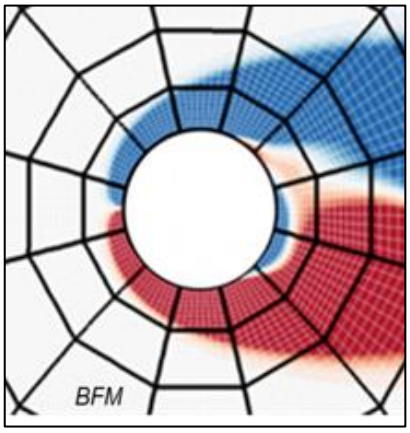


Figure 2.2 Boundary Fitted Method

IBM is a better choice for moving geometries (e.g. particle flows, fluid-structure interactionparticle flows) because the mesh does not have to move. A simple example is shown in Figure 2.3.

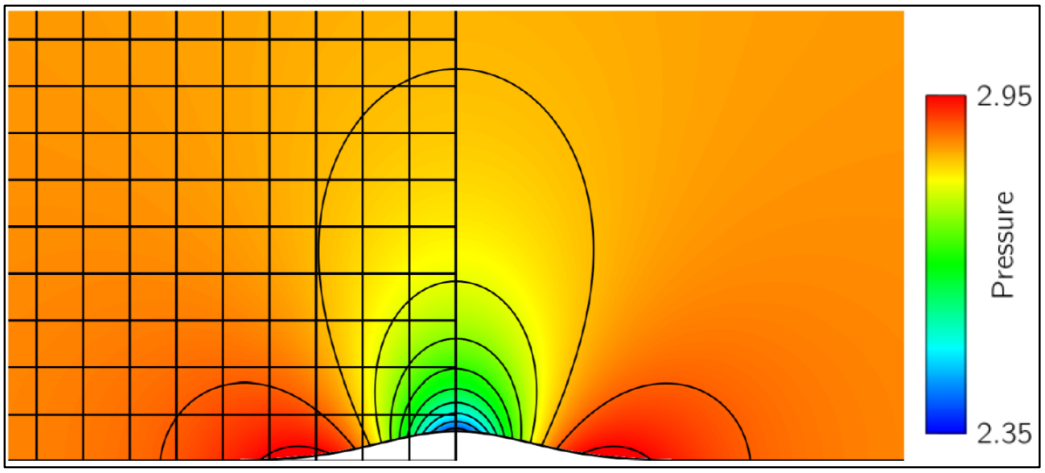


Figure 2.3 Compressible flow simulation, computed with Immersed Boundary Method (IBM) [7]

For this thesis, only explicit Euler time discretization for immersed boundary problems is used since all process are in the steady state.

2.2 Compressible Flow

Between this section and Chapter 4, the thesis is based entirely on [2] and [8]; slightly [9]. This section is based on [2].

Compressible flow is usually defined by variable density. Conversely, incompressible flow is defined by invariant density. It is clear that in real life fluids can be compressed, more or less. Bernoulli has some approaches about this topic which are reliable usually whereas John D. Anderson has other approaches either.

Bernoulli`s reliable equation:

$$p + \frac{1}{2}\rho V^2 = constant \tag{2.1}$$

Variable density needs to be more closely investigated. Consider a small volume "v", the pressure from the neighbor cells is "p". And now consider that the pressure is reduced to minimum size, dp. Correspondingly, the volume is compressed up to dv. Since the volume gets smaller, it starts to have minus values.

Compressibility of fluids:

$$\tau = -\frac{1}{v}\frac{dv}{dp} \tag{2.2}$$

In the Equation (2.2), v means any small volume and dv means compressed volume. Also dp means minimum pressure applied by neighbor cells. The reason of the negative (-) sign is that dv becomes negative while it is getting smaller during the compression process.

It is shown from gases that the temperature increases during the compression process. For all that, increasing of the system energy depends on the existence a heat transfer through the boundaries of the system. If the temperature of the fluid remains constant, the compressibility is called as "Isothermal".

Isothermal compressibility:

$$\tau_T = -\frac{1}{v}\left(\frac{\partial v}{\partial p}\right)_T \tag{2.3}$$

On the other hand, if the system does not have any heat transfer (adiabatic system) or any dissipative transport mechanism (reversible system) (for example viscosity and diffusion are important parameters at that point), the process of the mentioned compression becomes "Isentropic".

Isentropic compressibility:

$$\tau_s = -\frac{1}{v}\left(\frac{\partial v}{\partial p}\right)_s \tag{2.4}$$

Compressibility is a property of the fluid as liquids have very low and gases have high values (compressibility for water is $5x10^{-10}$ m^2/N at 1 atm and compressibility for air is 10^{-5} m^2/N at 1 atm). v is the specific volume (volume per unit mass), and the density is $\rho = 1/v$ with the assumption that the fluid elements have unit mass. Under these conditions;

$$\rho a = (\rho + d\rho)\,(a + da) \tag{2.5}$$

Consider that the fluid is not stable. A force, which appears usually due to the changes in pressure, starts and resumes this movement. In this situation, large pressure gradients are observed and it is more obvious during the high-speed flows. Equation (2.5) shows that gases are more affected by density changing than fluids. Therefore, the large pressure gradients of fluid flows can increase the velocity without considerably changing the density. For this reason, fluids are assumed as incompressible. If these changes of pressure cause large velocity changes or the density change is more than 5%, the flow is seen as compressible.

Speed of gases are less than about 0.3 of the speed of sound. This is associated with small changes of pressure, nevertheless compressibility is high for gases [2].

2.2.1 Speed of Sound and Mach Number

It is more accurate to understand the sound wave and Mach number first so that the shock wave can be understood better.

2.2.1.1 Speed of Sound

Consider the stagnant air for defining the speed of sound. The air is made up of molecules which move at different speeds and in random motion. The properties for perfect gas are functions of only temperature [2]. Then imagine a small firecracker detonates. The released energy from detonation is absorbed by the neighbor air molecules [2]. The molecules which have faster speed transfer some of the new energy they gained to the surrounding molecules with the help of colliding. Followed by this transfer, neighbors collide with the other neighbors and as a consequence, it is ensured that the firecrackers energy is transmitted or spread out clearly. This formation is sensed

as “sound” by our brain. Such a weak wave, which is mentioned, is defined as a sound wave.

Consider that the sound wave is moving with velocity a through the gas and imagine we are moving with it. As we move along with the wave, we see that the air in front of the wave is moving toward the wave at the velocity a [2], as shown in Figure 2.4.

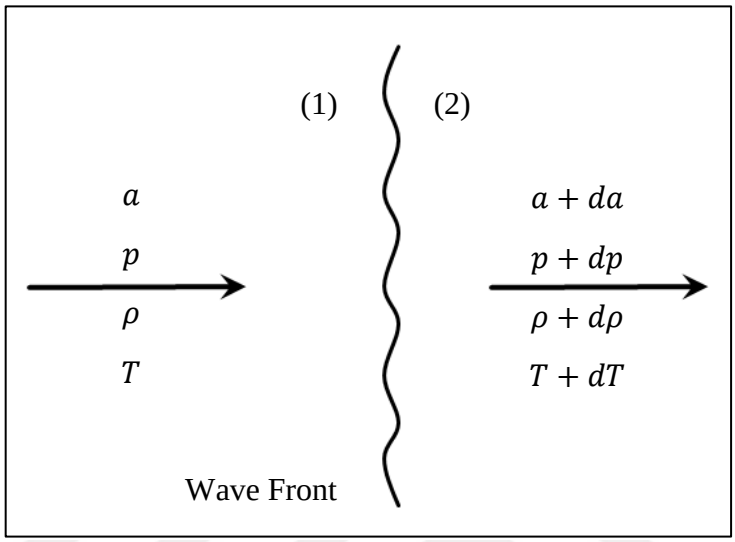


Figure 2.4 Schematic of a sound wave, based on [2]

Since there are changes in the flow properties along the wave, the flow behind the wave moves away at a different rate. However, these changes are small because a sound wave is a weak wave. The flow ahead of it moves toward the wave at velocity a and the flow behind it moves away from the wave at velocity $a + da$. The remaining properties ahead of shock wave are pressure, density, and temperature; p, ρ, and T, and behind it are $p + dp$, $\rho + d\rho$ and $T + dT$, respectively [2].

The flow through the sound wave is one-dimensional and therefore the following equations can be applied which are based on Figure 2.4:

$$\rho a = (\rho + d\rho)(a + da)$$
$$\rho a = \rho a + a d\rho + \rho da + d\rho da \tag{2.6}$$

If the equations are simplified with the help of too low value of $d\rho da$ foresight and momentum equation for steady one-dimensional flow:

$$a^2 = \frac{dp}{d\rho} \tag{2.7}$$

With the following assumptions and equations, which are based on [2], the final equation of sound velocity, Equation (2.8), is obtained:

- Irreversible, dissipative effects of friction and thermal conduction are negligible.
- There is no heat addition (laser, heater etc.) to the flow inside the wave. The process inside the sound wave must be isentropic.
- $\rho = \frac{1}{v}, \quad \gamma = {C_p}/{C_v}, \quad pv^{\gamma} = c\ (constant), \quad p/\rho = RT$

$$a = \sqrt{\gamma RT} \tag{2.8}$$

The speed of sound in air at standard sea level conditions is $a_s = 340.9\ m/s = \ 1117 ft/s$.

2.2.1.2 Mach Number

Consider far upstream of the body in Figure 2.5, the flow is uniform with a free stream velocity of V_∞. A streamline is a curve in the flow field and the flow field is tangent to the local velocity vector V at every point along the curve. If a is the speed of sound in the uniform free stream, the Mach number is described with the value V/a. $M = V/a$ varies from point to point in the flow field. If the speed of sound the uniform free stream, a_∞, is used, the V_∞/a_∞ value defines M_∞, the free stream Mach number which leads to the following general classifications of different flow regimes [2]:

- $M < 1 \ : \ Subsonic\ Flow$
- $M = 1 \ : \ Sonic\ Flow$
- $M > 1 \ : \ Supersonic\ Flow$

2.2.2 Flow Regimes

The successful manned flight began on 17th December 1903, with Orville and Wilbur Wright. They flew in their historic Flyer I. These experiments continued to the present with subsonic and supersonic airplanes. In the twentieth century, manned flight has been an induce factor for the development of fluid dynamics and compressible flow. As a conclusion of this, compressible flow knowledge can be used for whole of modern engineering problems. We also observe this frequently while investigating

aerodynamics and propulsion geared to airplanes and missiles [2]. To further visible different regimes of compressible flow, aerodynamic bodies in a flowing gas shown in Figure 2.5.

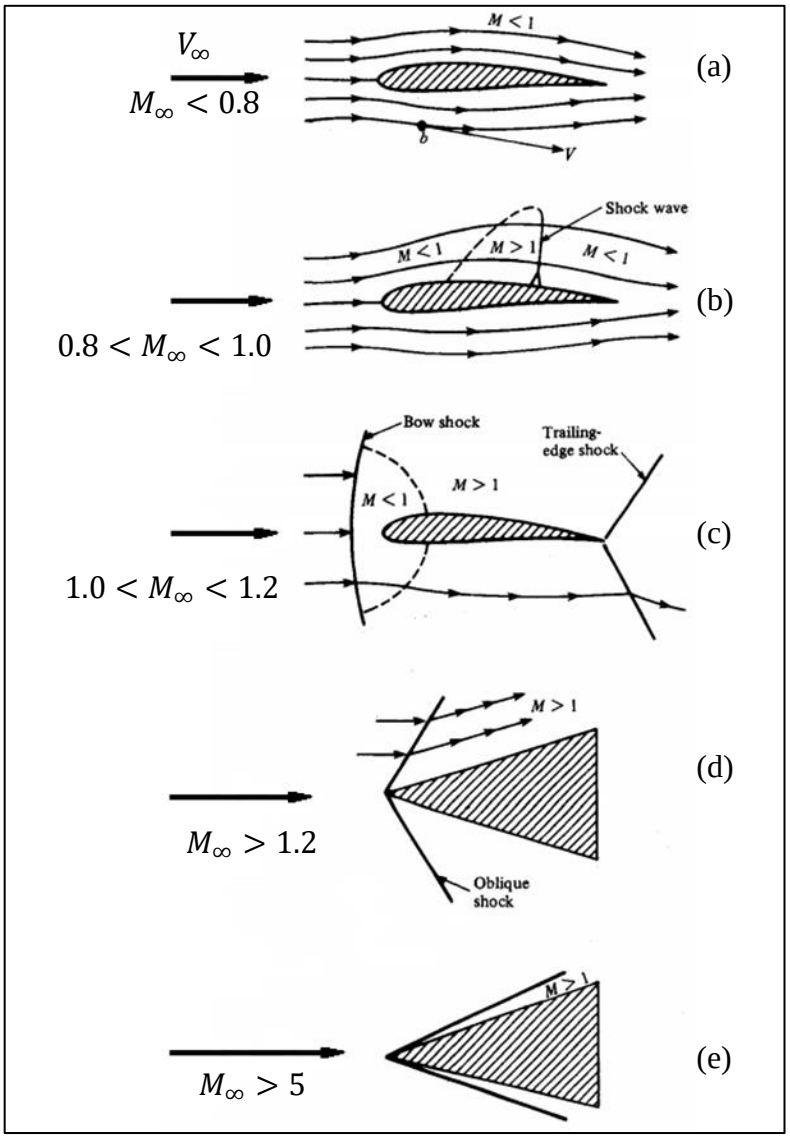


Figure 2.5 Illustration of different regimes of flow [2]

In Figure 2.5, some of the effects of infinite Mach number around a body are shown. Consider an arbitrary point in the flow field and at that point; P, T, ρ and V are the local pressure, temperature, density, and vector velocity. All of these quantities have different values from one point to another in the flow.

2.2.2.1 Subsonic Flow

Consider the flow in Figure 2.5 (a), at every point it is $M < 1$ so flow velocity is less than the speed of sound everywhere [8]. These kind of flows are defined as subsonic

flow. Subsonic flows are known with smooth streamlines and continuously varying properties. It can be seen that the streamlines, which are straight and parallel in the beginning, begin to deflect before meeting with surface, it implies that the flow is aware of the presence of the body. It should be noted that while the flow passes through the surface, the local velocity and Mach number on the top surface increase above their free stream values. But with this, if M can remain low enough, the local Mach number stays subsonic everywhere. $M_\infty \leq 0.8$ implies that the flow area is completely subsonic [2].

2.2.2.2 Transonic Flow

If M_∞ remains subsonic, but is sufficiently near 1, some irregularities can occur. As shown as Figure 2.5 (b), locally supersonic regions over the top surface can be observed. $M < 1$ requirement is appropriate for subsonic flow, neverthless the Mach number is high enough for observing some local supersonic areas. These areas can be formed by changes in flow properties or a shock wave which has some discontinuities. If M_∞ is more increased and getting over the value 1 slightly, two shock waves are observed as shown in Figure 2.5 (c). In that condition, as already aforementioned the shock will move to the trailing edge and a second shock wave appears upstream of the leading edge. The mentioned second shock wave is called "Bow Shock" [2]. The streamlines between these two shocks, which have a uniform supersonic free stream Mach number, are straight and parallel. Bow shock is just about perpendicular to the free stream. The flow becomes subsonic while passing through bow shock. Before long, the flow becomes supersonic again and ends with the trailing edge shock. In the epitome, Figure 2.5 (b) and (c) show mixed regions of locally subsonic and supersonic flow. These mixed flows are defined as transonic flows and M_∞ value is between 0.8 and 1.2 [2].

2.2.2.3 Supersonic Flow

If the flow's Mach number is $M > 1$ everywhere in the flow field, that flow is defined as supersonic. Consider the flow and the wedge-shaped body in Figure 2.5 (d). A straight, oblique shock wave is attached to the sharp nose and the streamline direction changes discontinuously. The streamlines which are straight, parallel and horizontal in the beginning, begin to deflect when they meet with the surface because of the occurrence of a shock wave. It implies that the flow is not aware of the presence of the

body unlike the subsonic flow in Figure 2.5 (a). After the shock wave, streamlines are still straight and parallel but in the direction of the wedge surface [2].

2.2.2.4 Hypersonic Flow

When hypersonic flow is concerned, huge differences variations temperature, pressure and density of flow are observed. In these properties, sudden and extreme increasing is observed across the shock wave. With further increase of M, the mentioned sudden and extreme increase becomes severe. Hypersonic flow is showed in Figure 2.5 (e) and as seen, the oblique shock wave moves closer to the surface than in Figure 2.5 (d), supersonic flow when Mach number is over the value 5. The shock wave comes significantly closer to the surface of the body and the flow area between the shock and the body becomes very hot. This area becomes hot enough to dissociate or ionize the gas. The flow in the mentioned area becomes more complicated to analyze as a result of the chemical reactions caused by high temperature. Under these conditions, the flow is described as hypersonic and choosing $M_\infty = 5$ as a dividing point between supersonic and hypersonic flow is a rule of thumb [2].

CHAPTER 3

SHOCK WAVES AND SHOCK WAVE REFLECTIONS

In this chapter, shock waves will be described first. After understanding the meaning of shock waves, shock wave reflections will be explained for describing Double Mach Reflection later.

3.1 Shock Waves

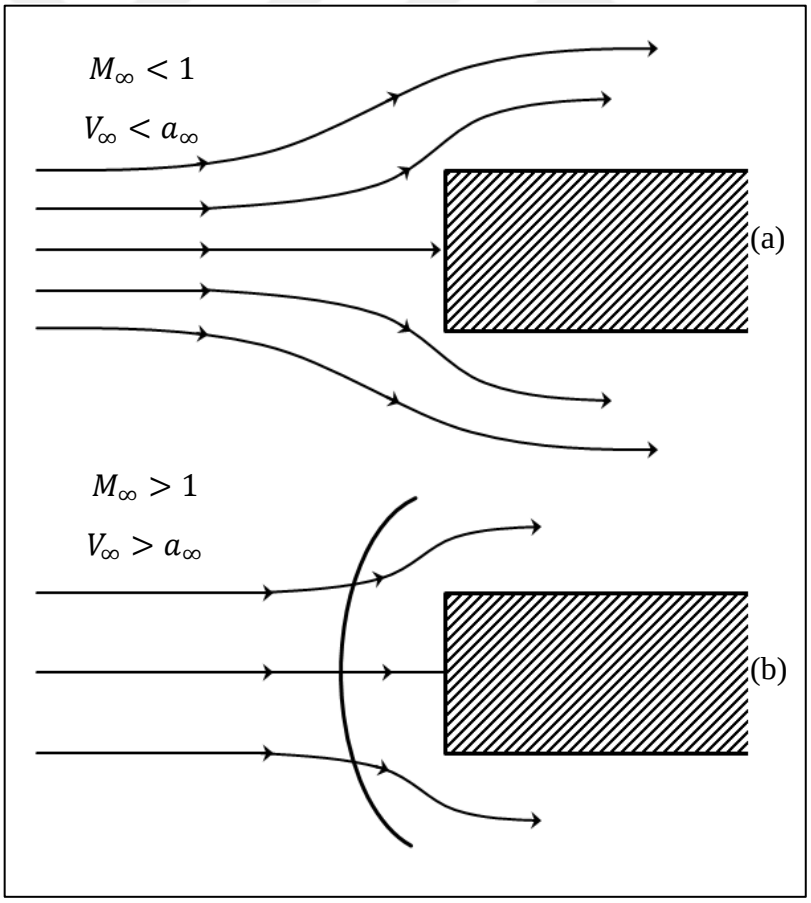


Figure 3.1 Comparison between subsonic and supersonic streamlines for flow over a flat-faced cylinder or slab, based on [2]

If there is a structure in a supersonic flow, shock waves are inevitable. The main reason for this is finding a solution to that complex problem about the propagation of disturbances in the flow. For understanding better, a flat faced cylinder mounted in a flow is sketched in Figure 3.1. There is a general changing in molecular energy and momentum due to impact with the cylinder which is seen as an obstruction by the flow molecules [2]. This situation is similar to Section 2.2.1 which investigated the creation of a sound wave. The random motion of the molecules transmits this change in energy and momentum to neighbors of these molecules. As shown in Figure 3.1 (a), the flow streamlines begin to change and the flow properties begin to compensate for the body far upstream (theoretically, an infinite distance upstream). But the sound waves can no longer propagate upstream if the flow is supersonic, namely that means $V_\infty > a_\infty$. Instead of this, they tend to develop a coalesce forms which is a thin shock, a short distance ahead of the body. Under these conditions, the flow cannot realize the existence of the structure ahead of the shock wave [9]. The picture, which is shown in Figure 3.1 (b), is only one of many situations in which nature creates shock waves, nevertheless the physical mechanism is quite general [2].

Near the sharp nose which exists on the body, this resulting wave is nearly perpendicular (normal) to the flow and is called a normal shock. The shock becomes oblique gradually in the area which is away from the nose. Oblique waves that occur in supersonic flow and oblique shocks usually occur when supersonic flow is "turned into itself" or "turned away from itself" as shown in Figure 3.4. Normal shock is one kind of a general family of oblique shocks [9].

3.1.1 One-dimensional Phenomena: Normal Shock Waves

One-dimensional flow is the flow whose properties vary only with one coordinate direction. Normal shock is an example of one-dimensional flow and shown in Figure 3.2. P, ρ, T and u are functions of only x [8].

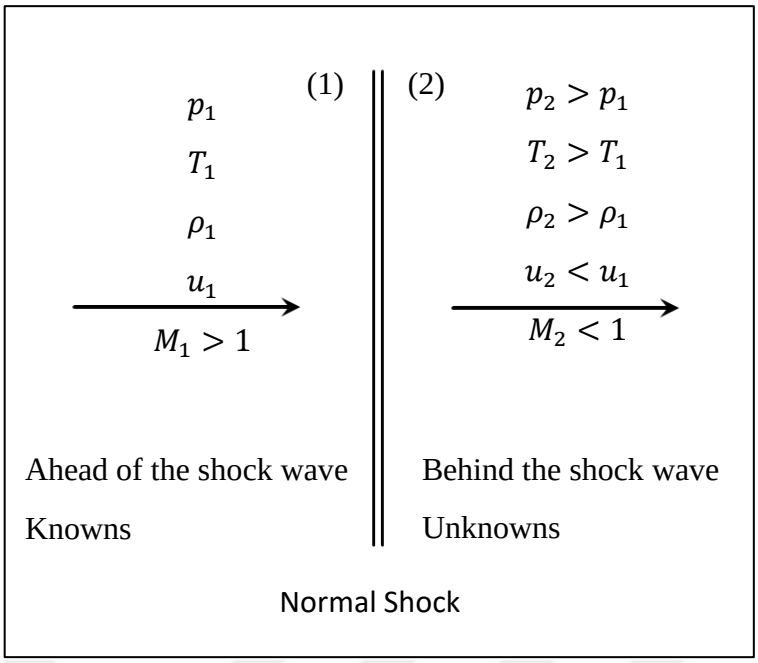


Figure 3.2 Diagram of a normal shock, based on [8]

3.1.1.1 One-dimensional Flow Equations

The flow properties on the left side of this region, namely the flow field velocity, pressure, temperature, density, and internal energy are u_1, p_1, T_1, ρ_1 and e_1 respectively. On the right side of this region, the properties are changed and expressed by u_2, p_2, T_2, ρ_2 and e_2. The velocity is named u because we are dealing with one-dimensional flow at this point. As you will see later on, in dealing with multidimensional flows, u is the x component of velocity V. Due to one-dimensional flow, the properties are uniform on both sides amongst themselves. Assume an area A on the left and right side respectively which is perpendicular to the flow. Furthermore, assume the flow to be steady and the absence of body forces. As a result of these assumptions, all derivatives with respect to time are zero. In the end, the continuity, momentum and energy equations, which are quite general because they apply to all flows, even compressible or incompressible, viscous or inviscid, become Equations (3.2), (3.4) and (3.7).

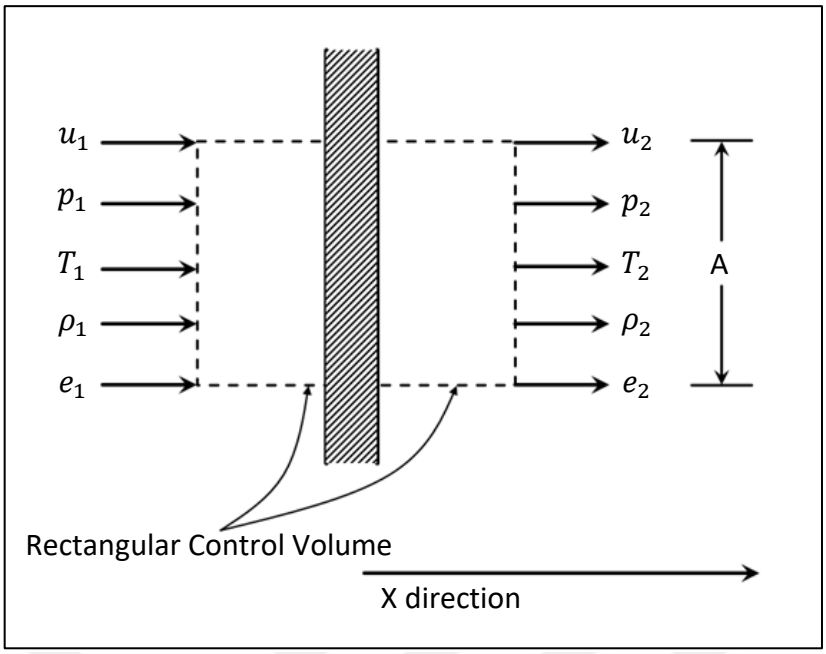


Figure 3.3 Rectangular control volume for one-dimensional flow, based on [2]

Continuity equation for general:

$$\oiint_S \rho V.dS = \frac{\partial}{\partial t} \iiint_{\bar{V}} \rho d\bar{V} \tag{3.1}$$

V, S and $\bar{V}$ are velocity, area and volume, respectively. Since we are dealing with one-dimensional flow, we need to consider only the scalar x component. V and dS are parallel on the right side but in opposite directions on the left side so they become respectively: $-\rho_1 u_1 A$ and $\rho_2 u_2 A$.

Continuity equation for steady one-dimensional flow:

$$-\rho_1 u_1 A + \rho_2 u_2 A = 0$$
$$\rho_1 u_1 = \rho_2 u_2 \tag{3.2}$$

Momentum equation for general:

$$\oiint_S (\rho V.dS)V + \iiint_{\bar{V}} \frac{\partial(\rho V)}{\partial t} d\bar{V} = \iiint_{\bar{V}} \rho f d\bar{V} - \oiint_S p dS \tag{3.3}$$

f is force per unit mass and equal to $\rho d\bar{V}$. The second and third term are zero because we consider steady flow and there are no body forces.

Momentum equation for steady one-dimensional flow:

$$\rho_1(-u_1 A)u_1 + \rho_2(u_2 A)u_2 = -(-p_1 A + p_2 A) \tag{3.4}$$

$$p_1 + \rho_1 {u_1}^2 = p_2 + \rho_2 {u_2}^2$$

Energy equation for general:

$$\iiint_{\bar{V}} \dot{q}\rho d\bar{V} - \iint_S pV.dS + \iiint_{\bar{V}} \rho(f.V)d\bar{V} = \iiint_{\bar{V}} \frac{\partial}{\partial t}\left[\rho\left(e + \frac{V^2}{2}\right)\right]d\bar{V} + \iint_S \rho\left(e + \frac{V^2}{2}\right)V.dS \tag{3.5}$$

Consider the first term which can be also expressed shortly as $\dot{Q}$. This term expresses the total rate of heat conducted to the gas inside the control volume. The third and fourth terms are zero because body forces do not exist and due to steady flow, respectively [2].

$$\frac{\dot{Q}}{\rho_1 u_1 A} + \frac{p_1}{\rho_1} + e_1 + \frac{{u_1}^2}{2} = \frac{p_2}{\rho_2} + e_2 + \frac{{u_2}^2}{2} \tag{3.6}$$

$\dot{Q}$ is the net rate of heat $(energy/s)$ added to the control volume, and $\rho_1 u_1 A$ represents the mass flow $(mass/s)$ through the control volume. As a result of this, the ratio $\dot{Q}/\rho_1 u_1 A$ is simply the heat added per unit mass, q. Additionally, considering the enthalpy is $h = e + pv$, Equation (3.6) becomes Equation (3.7) [2].

Energy equation for steady one-dimensional flow:

$$h_1 + \frac{{u_1}^2}{2} + q = h_2 + \frac{{u_2}^2}{2} \tag{3.7}$$

3.1.1.2 Normal Shock Relations

A normal shock wave is defined by its perpendicularity to the flow, as seen in Figure 3.2. The shock is a very thin region and the shock thickness is typically $10^{-5}cm$ for air at standard conditions. The flow is supersonic ahead of the wave, and subsonic behind it. Furthermore, the static pressure, temperature, and density increase whereas the velocity decreases across the shock [9]. For understanding better, a flat faced cylinder mounted in a flow is sketched in Figure 3.1. The cylinder is seen as an obstacle by the flow and as a cause of this, a general changing in molecular energy and momentum occurs. Remember the Section 2.2.1 which investigated the form of the sound wave which is related to this situation. The neighbor molecules are affected by the change in energy and momentum which are the result of the random motion of the molecules. As

shown in Figure 3.1 (a), the flow streamlines begin to change and the flow properties begin to compensate for the body far upstream (theoretically, an infinite distance upstream) [2].

Handle with care again that the field on the left side is named region (1) and right side is named region (2) in Figure 3.2. There is not any heat transfer from the flow (laser etc. do not exist). Therefore, the basic normal shock equations are obtained directly [2] as mentioned in Section 3.1.1.1.

- Continuity $\rho_1 u_1 = \rho_2 u_2$
- Momentum $p_1 + \rho_1 {u_1}^2 = p_2 + \rho_2 {u_2}^2$
- Energy $h_1 + \frac{{u_1}^2}{2} + q = h_2 + \frac{{u_2}^2}{2}$

However, for a calorically perfect gas, we can use some thermodynamic relations. If we recall that $a = \sqrt{\gamma p/\rho}$ and use some assumptions [2]; we obtain an equation which gives a relation between the Mach numbers in field (1) and (2).

$$ {M_2}^2 = \frac{1 + [\frac{\gamma - 1}{2}]{M_1}^2}{\gamma {M_1}^2 - [\frac{\gamma - 1}{2}]} \tag{3.8} $$

3.1.2 Two-dimensional Phenomena: Oblique Shock Wave

Oblique shock waves are two or three-dimensional phenomena. This study includes only two-dimensional oblique shock waves. As mentioned in Section 3.1, oblique shocks usually occur when supersonic flow is "turned into itself" or "turned away from itself". If it is turning away from itself, the shock waves are called oblique expansion shock as shown in Figure 3.4 (b). For understanding the mechanism of oblique shock, consider Figure 3.4 (a). This figure shows an originally uniform supersonic flow. Starting with point A, there is a deflected surface upward with angle θ. As a result of this, streamlines deflect upward after shock wave and this situation is observed all along the wave. Across the shock wave; the pressure, temperature, and density increase and the Mach number decreases [2].

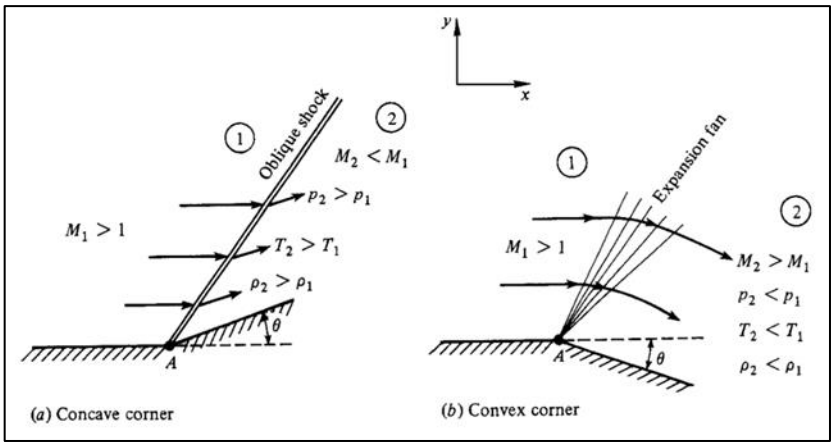


Figure 3.4 Supersonic flow over a corner [2]

Consider a point source of sound in a gas which is moving with the speed V as seen in Figure 3.5. This point is called "beeper" [2]. If the speed of beeper, V, is lower than speed of sound, a, Figure 3.5 (a) is observed and if higher, Figure 3.5 (b) is observed.

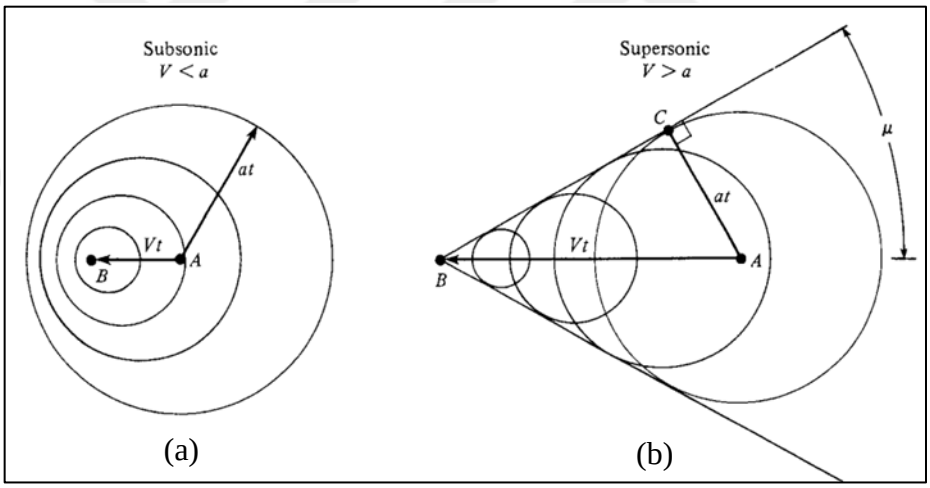


Figure 3.5 The propagation of disturbances in (a) subsonic and (b) supersonic flow [2]

In Figure 3.5 (b), a different phenomenon can be observed; these wave fronts form a disturbance given by the straight line BC, which is tangent to the family of circles. This line is defined as a Mach wave and the angle ABC is defined as the Mach angle, μ [2].

Consider a body with sharp nose as shown in Figure 3.6. If the disturbance which is mentioned before is stronger than a small beeper emitting sound waves, such as a wedge blasting its way through a gas at supersonic speeds, the wave front becomes stronger than a Mach wave. The strong disturbances coalesce with the angle β which has higher angle than Mach angle [9].

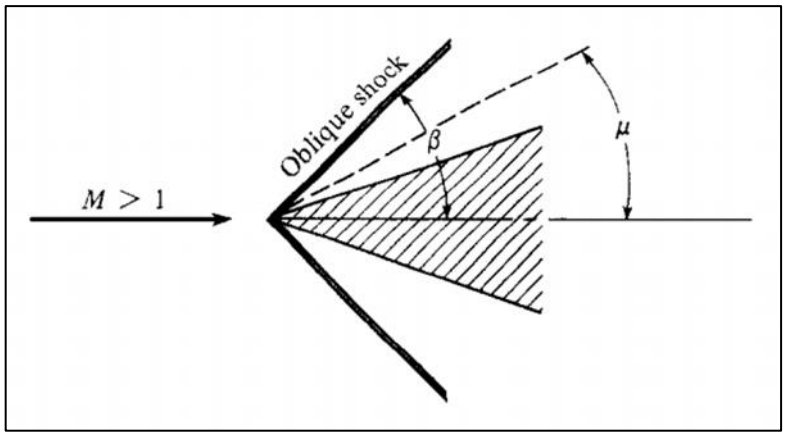


Figure 3.6 Comparison between the wave angle and the Mach angle [2]

3.1.2.1 Oblique Shock Relations

The geometry of an oblique shock is shown in Figure 3.7. V_1 is the velocity upstream of the shock and is horizontal. In the flow field (1) the appropriate Mach number is M_1. The shock which has the angle β, deflect the stream lines with the angle θ.

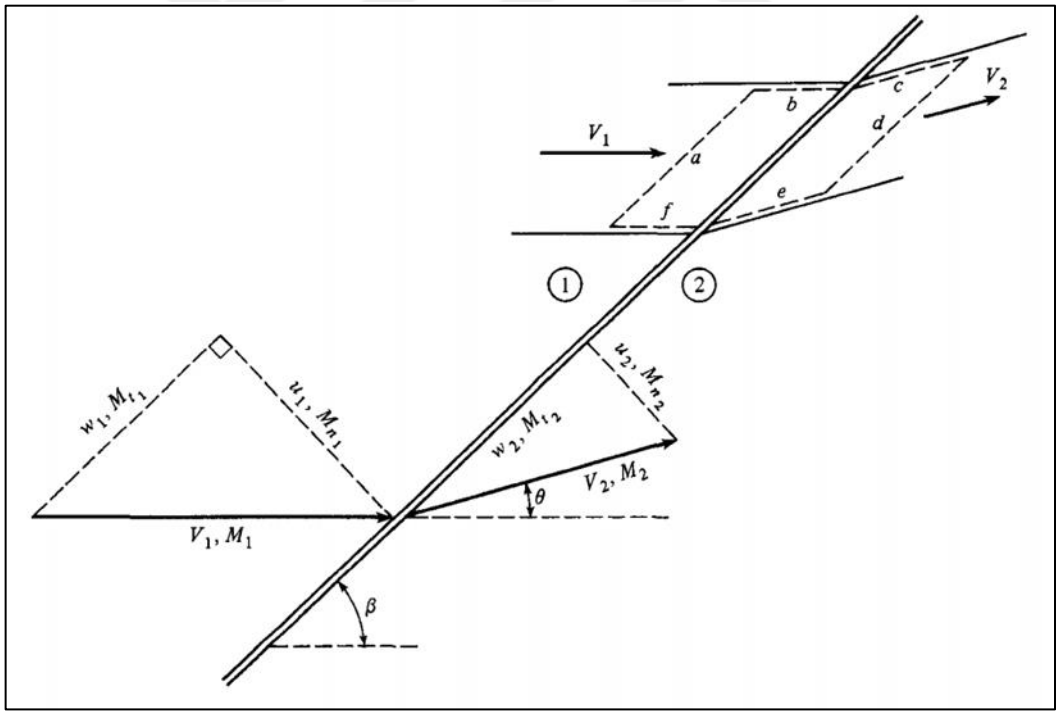


Figure 3.7 Oblique shock wave geometry [2]

The properties in front of and behind the shock wave are illustrated in Figure 3.7. These are velocities V_1, V_2; Mach numbers M_1, M_2; components of velocity u_1, w_1, u_2, w_2; components of the Mach number M_{n_1}, M_{t_1}, M_{n_2}, M_{t_2}.

Looking back to the one-dimensional equations for normal shock wave, we observe that oblique shock wave relations have similar simplifications and the same continuity, momentum and energy equations. The reason of this similarity despite the oblique shock wave with deflected angle is that normal components are used for these equations. In addition, after simplifications, we obtain $w_1 = w_2$ with the help from momentum equation:

$$(-\rho_1 u_1)w_1 + (\rho_2 u_2)w_2 = 0 \tag{3.9}$$

- Continuity $\rho_1 u_1 = \rho_2 u_2$
- Momentum $p_1 + \rho_1 {u_1}^2 = p_2 + \rho_2 {u_2}^2$
- Energy $h_1 + \frac{{u_1}^2}{2} + q = h_2 + \frac{{u_2}^2}{2}$

For a calorically perfect gas, the remaining equations are:

$$M_{n_1} = M_1 sin\beta \tag{3.10}$$

$$\frac{\rho_2}{\rho_1} = \frac{(\gamma+1){M_{n_1}}^2}{(\gamma-1){M_{n_1}}^2 + 2} \tag{3.11}$$

$$\frac{p_2}{p_1} = 1 + \frac{2\gamma}{(\gamma+1)}({M_{n_1}}^2 - 1) \tag{3.12}$$

$${M_{n_2}}^2 = \frac{{M_{n_1}}^2 + [2/(\gamma-1)]}{[2\gamma/(\gamma-1)]{M_{n_1}}^2 - 1} \tag{3.13}$$

$$\frac{T_2}{T_1} = \frac{\rho_2}{\rho_1}\,\frac{p_1}{p_2} \tag{3.14}$$

$$M_2 = \frac{M_{n_2}}{\sin(\beta-\theta)} \tag{3.15}$$

Normal shocks are only a special case of oblique shocks where $\beta = \pi/2$. With some trigonometric manipulations we obtain the equation which has $\beta - \theta - M$ relation.

$$tan\theta = 2cot\beta\left[\frac{M_1^2 sin^2\beta - 1}{M_1^2(\gamma + cos2\beta) + 2}\right] \tag{3.16}$$

There are differences in shock waves according to the angles θ and β; and M_1. For any given M_1, there is a maximum deflection angle θ_{max}. If $\theta > \theta_{max}$, no solution exists for a straight oblique shock wave, it becomes detached and curved. If $\theta < \theta_{max}$, there are two kind of shock wave which can exist: strong or weak wave. For large values of β the wave is called strong wave and M_2 is known to be subsonic. For weak shocks M_2 is

supersonic except for a small region near θ_{max}. The described strong and weak shock waves are illustrated in Figure 3.8.

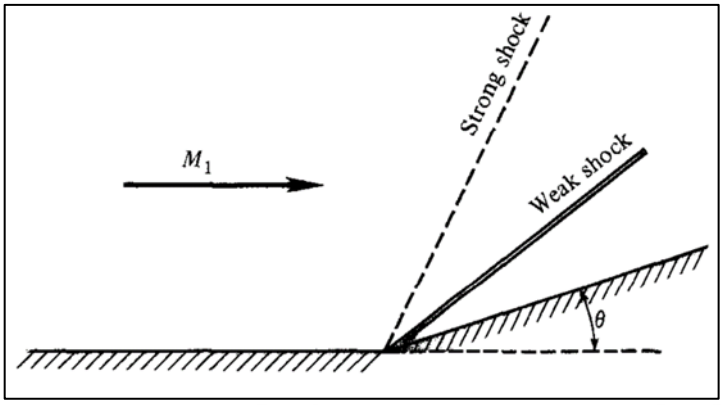


Figure 3.8 Weak and strong shocks [2]

Consider that deflection angle θ is fixed. The wave angle β increases while Mach number decreases provided that staying supersonic values. However, there is a Mach number value which has no solution due to $\theta = \theta_{max}$. For lower Mach numbers, the shock becomes detached [2]. The detached-attached and straight-curved shock waves described so far are summarized in Figure 3.9.

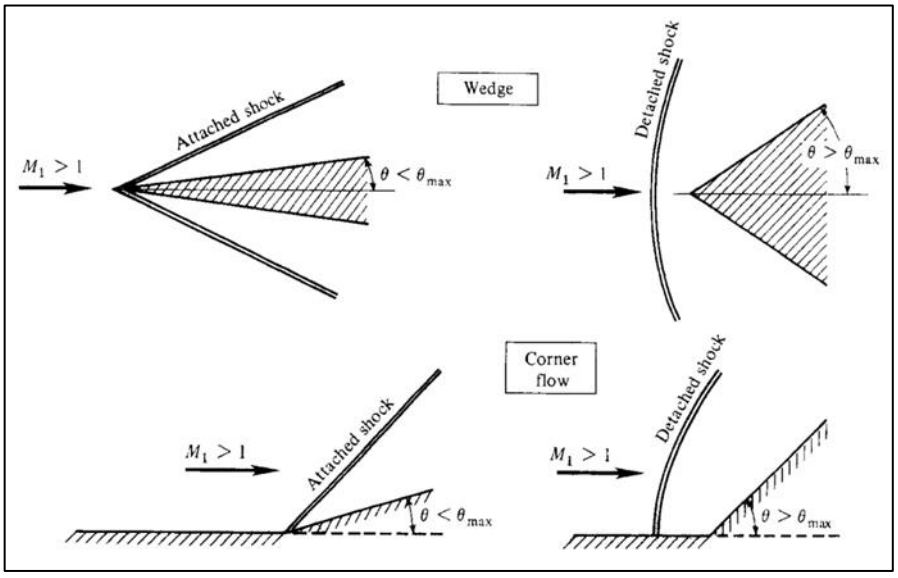


Figure 3.9 Attached and detached shocks [2]

If we consider Figure 3.10 and Equations (3.9) to (3.16), for example it is clear to see, with fixed Mach number, while θ is increased; β, p_2, T_2, and ρ_2 increase and M_2 decreases. However, in case $\theta > \theta_{max}$, we observe the shock wave becomes detached

anymore. With fixed θ, while M_1 increases, the shock wave is first detached, then becomes attached when M_1 equals that value for which $\theta = \theta_{max}$. If Mach number increases further, the shock remains attached and β decreases; p_2, T_2, ρ_2, and M_2 increase [2].

It can be found out what is mentioned about oblique shock before, as partially summarized in Figure 3.10.

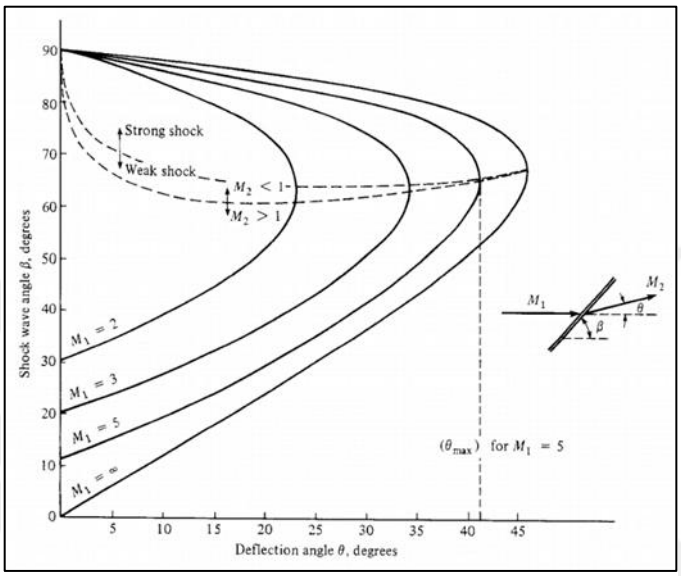


Figure 3.10 θ-β-M curves. Oblique shock properties [2]

3.2 Shock Wave Reflections

This section is based on Ben-Dor [9] with all equations.

In fine, two types of shock wave reflections are available:

- Regular Reflection (RR)
- Irregular Reflection (IR)

A Regular Reflection (RR) includes two kind of shock waves; an incident shock wave (i) and a reflected shock wave (r). The intersection point of the two named shock waves is defines as "Reflection Point (R)". All other kind of shock wave reflections are referred to as "Irregular Reflection (IR)".

Mach Reflection (MR) which is one kind of Irregular Reflections includes three kind of shock waves; incident shock wave (i), reflected shock wave (r), Mach stem (m) and additionally it has a slip line (s). These four discontinuities' intersection point is called "Triple Point (T)" which exist over the reflective surface. As seen on the Figure 3.15,

there is a visible discontinuity between incident shock wave and Mach reflection. Under these conditions the reflection point (R) is the point at which the reflective surface and Mach stem meet. Mach stem is assumed perpendicular to the reflective surface.

To explain briefly, there are 13 different possible wave configurations and they are associated with the reflection of a shock wave over an oblique surface. To make it clearer, these 13 different possible wave configurations which include Double Mach Reflection are shown in Figure 3.11.

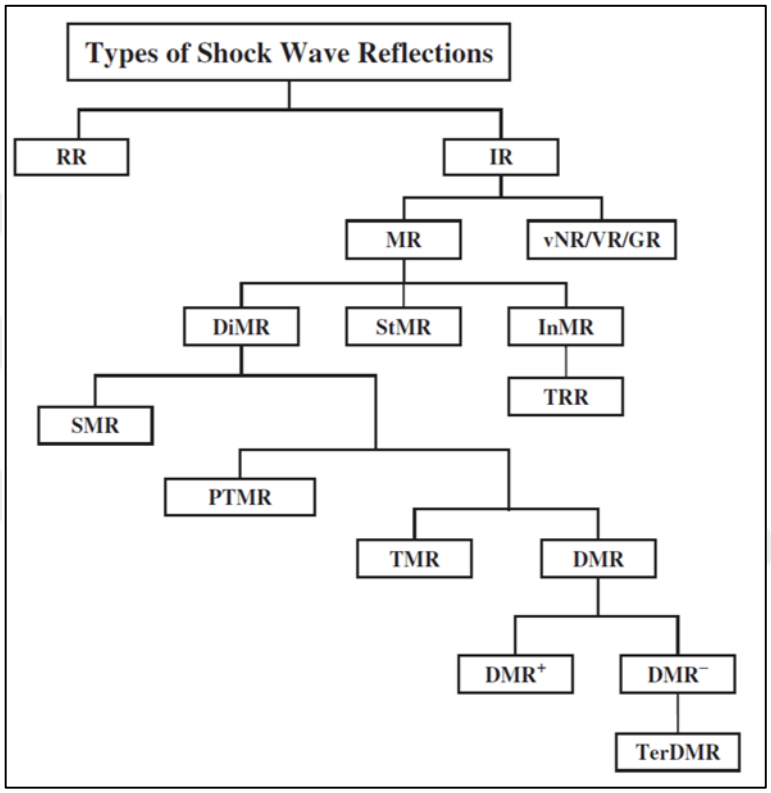


Figure 3.11 The 13 possible shock wave reflection configurations [9]

3.2.1 Reasons for the Reflections

Figure 3.12 includes three different cases with different initial Mach number M_0 and wedge angle θ_w.

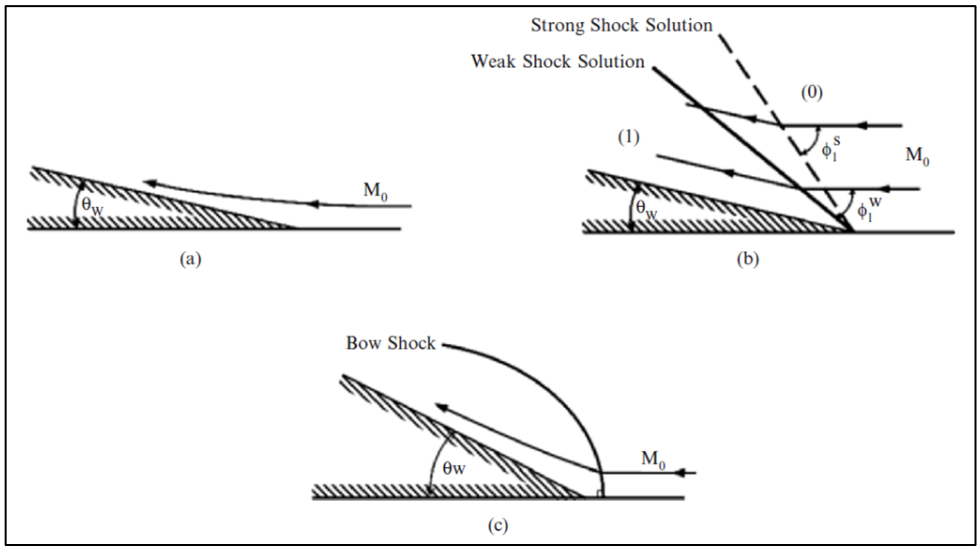


Figure 3.12 Flow over a wedge in a steady flow: (a) $M_0 < 1$, smooth subsonic turning; (b) $M_0 > 1$ and $\theta_w < \theta_{max}(M_0)$, straight and attached oblique shock wave; (c) $M_0 > 1$ and $\theta_w > \theta_{max}(M_0)$, detached curved (bow) shock wave [9]

In the first case, in Figure 3.12 (a), the flow is subsonic, namely $M_0 < 1$. This implies that obstacle is well known by the flow and so the flow can adjust itself before meeting with surface with angle and it can hurdle the obstacle as subsonic. With all these, if the flow is supersonic, namely $M_0 > 1$, cannot realize the obstacle and so it has only one option for passing through the obstacle which is a with a shock wave occurring suddenly, as shown as in Figure 3.12 (b) and Figure 3.12 (c). Under these conditions, two cases are possible. One of them is straight and attached shock wave on account of the obstacle, but in that case the shock wave is still trying to stay parallel to the surface as shown as in Figure 3.12 (b). The other one is curved and detached shock wave, in that case along this surface the shock wave is turned from supersonic to subsonic as shown as in Figure 3.12 (c). The reason of the detached shock wave is that the attached oblique shock wave is impossible in case θ_w has higher value than the limit $\theta_{max}(M_0)$.

3.2.2 Analytical Approaches for Describing Regular and Mach Reflections

The analytical approaches for describing the RR and the MR wave configurations were initiated by Neumann (1943a and 1943b) [9]. The one describing the RR is known as the two-shock theory, 2ST. The other one for MR is known as the three-shock theory, 3ST. Both theories make use of the inviscid conservation equations across an oblique shock wave, together with appropriate boundary conditions.

Figure 3.13 includes an oblique shock wave with flow fields which were separated as ahead and behind the oblique shock wave, i and j, respectively. The angle between the oncoming flow u_i and the oblique shock wave is ϕ_j. The angle between the flow which passed through the oblique shock (u_j) and the trace of u_i is θ_j.

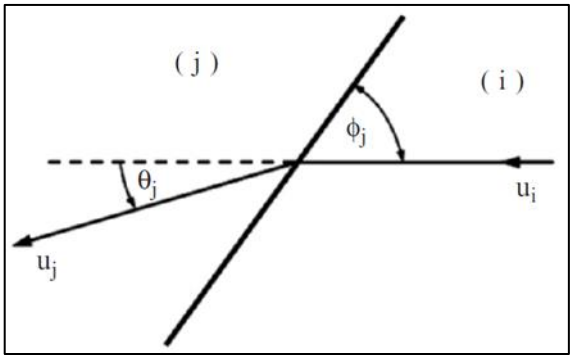


Figure 3.13 Definition of parameters across an oblique shock wave [9]

The conservation of mass:

$$\rho_i u_i sin\phi_j = \rho_j u_j sin(\phi_j - \theta_j) \tag{3.17}$$

The conservation of normal momentum:

$$p_i + \rho_i u_i^2 sin^2\phi_j = p_j + \rho_j u_j^2 sin^2(\phi_j - \theta_j) \tag{3.18}$$

The conservation of tangential momentum:

$$\rho_i tan\phi_j = \rho_j tan(\phi_j - \theta_j) \tag{3.19}$$

The conservation of energy:

$$h_i + \frac{1}{2}u_i^2 sin^2\phi_j = h_j + \frac{1}{2}u_j^2 sin^2(\phi_j - \theta_j) \tag{3.20}$$

u, ρ, p and h as seen in these equations are the flow velocity, flow density, flow static pressure and flow enthalpy, respectively. If thermodynamic equilibrium exists on both sides of the oblique shock wave, then two thermodynamic properties are sufficient to fully define a thermodynamic state, e.g., $\rho = \rho(p, T)$ and $h = h(p, T)$, where T is the flow temperature. With this assumption, these four equations includes eight parameters, namely, $p_i, p_j, T_i, T_j, u_i, u_j, \phi_j$ and θ_j. If four of these parameters are known, these conservation equations get solvable.

3.2.2.1 Two-Shock Theory (2ST) for an Inviscid Flow

This theory is an analytical model and developed for RR. The area near the reflection point R is defined with this theory. The RR consists of incident shock wave i and the reflected shock wave r. Figure 3.14 includes the wave configurations of an RR in an inviscid flow and some associated parameters.

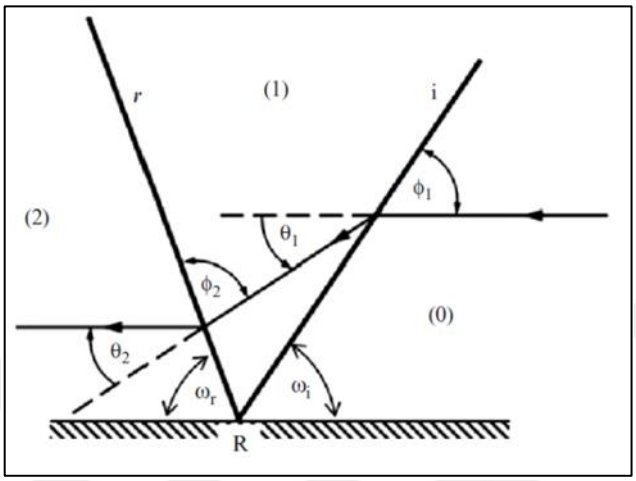


Figure 3.14 Schematic illustration of the wave configuration of a RR [9]

Shock wave reflection is not a linear process so RR wave configuration is not linear either. These two shock waves` meeting point is R which is located on the reflecting surface.

Across the incident shock wave, i:

$$\rho_0 u_0 sin\phi_1 = \rho_1 u_1 sin(\phi_1 - \theta_1) \tag{3.21}$$

$$p_0 + \rho_0 u_0^2 sin^2\phi_1 = p_1 + \rho_1 u_1^2 sin^2(\phi_1 - \theta_1) \tag{3.22}$$

$$\rho_0 tan\phi_1 = \rho_1 tan(\phi_1 - \theta_1) \tag{3.23}$$

$$h_0 + \frac{1}{2}u_0^2 sin^2\phi_1 = h_1 + \frac{1}{2}u_1^2 sin^2(\phi_1 - \theta_1) \tag{3.24}$$

Across the reflected shock wave, r:

$$\rho_1 u_1 sin\phi_2 = \rho_2 u_2 sin(\phi_2 - \theta_2) \tag{3.25}$$

$$p_1 + \rho_1 u_1^2 sin^2\phi_2 = p_2 + \rho_2 u_2^2 sin^2(\phi_2 - \theta_2) \tag{3.26}$$

$$\rho_1 tan\phi_2 = \rho_2 tan(\phi_2 - \theta_2) \tag{3.27}$$

$$h_1 + \frac{1}{2}u_1^2 sin^2\phi_2 = h_2 + \frac{1}{2}u_2^2 sin^2(\phi_2 - \theta_2) \tag{3.28}$$

In addition to the presented eight equations, the reflected wave which is located in area 2 should be parallel to the reflecting surface:

$$\theta_1 - \theta_2 = 0 \tag{3.29}$$

As a result, the area of near the reflection point R has nine governing equations.

Under the assumptions of thermodynamic equilibrium in states (0), (1), and (2); then density, ρ, and enthalpy, h, could be expressed in terms of the pressure, p, and the temperature, T, [i.e., $\rho = \rho(p,T)$ and $h = h(p,T)$]. With this thought, these nine governing equations have only 13 parameters: p_0, p_1, p_2, T_0, T_1, T_2, u_0, u_1 u_2, ρ_1, ρ_2, θ_1 and θ_2. Four of these 13 parameters must be known for solving these equations successfully.

3.2.2.2 Three-Shock Theory (3ST) for an Inviscid Flow

This theory is an analytical model and developed for Mach Reflection (MR). The area of near the reflection point R is defined with this theory. The MR consist of incident shock wave i, reflected shock wave r, Mach stem m and one slip line s. These four discontinuities' meeting point is T. Even though it is not much, Mach stem has a curve usually. It can be concave or convex, depending on the initial conditions. Mach stem and reflection surface's meeting point is R. Figure 3.15 includes the wave configurations of an MR in inviscid flow and some associated parameters.

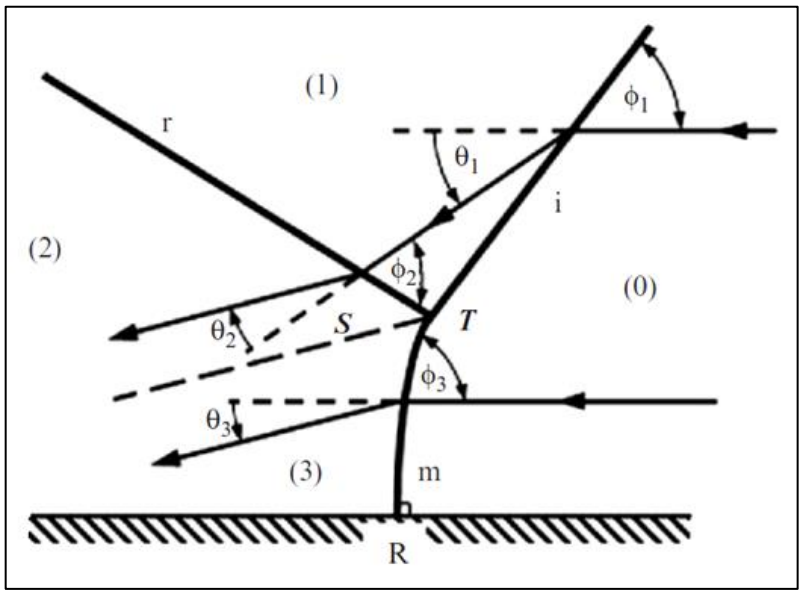


Figure 3.15 Schematic illustration of the wave configuration of an MR [9]

Across the incident shock wave, i:

$$\rho_0 u_0 sin\phi_1 = \rho_1 u_1 sin(\phi_1 - \theta_1) \quad (3.21)$$

$$p_0 + \rho_0 u_0^2 sin^2\phi_1 = p_1 + \rho_1 u_1^2 sin^2(\phi_1 - \theta_1) \quad (3.22)$$

$$\rho_0 tan\phi_1 = \rho_1 tan(\phi_1 - \theta_1) \quad (3.23)$$

$$h_0 + \frac{1}{2}u_0^2 sin^2\phi_1 = h_1 + \frac{1}{2}u_1^2 sin^2(\phi_1 - \theta_1) \quad (3.24)$$

Across the reflected shock wave, r:

$$\rho_1 u_1 sin\phi_2 = \rho_2 u_2 sin(\phi_2 - \theta_2) \quad (3.25)$$

$$p_1 + \rho_1 u_1^2 sin^2\phi_2 = p_2 + \rho_2 u_2^2 sin^2(\phi_2 - \theta_2) \quad (3.26)$$

$$\rho_1 tan\phi_2 = \rho_2 tan(\phi_2 - \theta_2) \quad (3.27)$$

$$h_1 + \frac{1}{2}u_1^2 sin^2\phi_2 = h_2 + \frac{1}{2}u_2^2 sin^2(\phi_2 - \theta_2) \quad (3.28)$$

Across the Mach stem, m:

$$\rho_0 u_0 sin\phi_3 = \rho_3 u_3 sin(\phi_3 - \theta_3) \quad (3.30)$$

$$p_0 + \rho_0 u_0^2 sin^2\phi_3 = p_3 + \rho_3 u_3^2 sin^2(\phi_3 - \theta_3) \quad (3.31)$$

$$\rho_0 tan\phi_3 = \rho_3 tan(\phi_3 - \theta_3) \quad (3.32)$$

$$h_0 + \frac{1}{2}u_0^2 sin^2\phi_3 = h_3 + \frac{1}{2}u_3^2 sin^2(\phi_3 - \theta_3) \quad (3.33)$$

In addition to the 12 equations above, the flow states (2) and (3) have the same pressure value. Because they are separated by a contact surface which the pressure remains constant across the reflected wave.

$$p_2 = p_3 \quad (3.34)$$

Moreover, under the assumptions of an inviscid flow and an infinitely thin contact surface the streamlines on both sides of the contact surface are parallel.

$$\theta_1 \mp \theta_2 = \theta_3 \quad (3.35)$$

This equation presents two more equations; one of them is called Standard Three Shock Theory (Equation (3.36)), and the other one is Nonstandard Three Shock Theory (Equation (3.37)).

$$\theta_1 - \theta_2 = \theta_3 \quad (3.36)$$

$$\theta_1 + \theta_2 = \theta_3 \quad (3.37)$$

The solution of the standard three-shock theory provides an MR, and the solution of the nonstandard three-shock theory provides a vNR.

As a result, the three-shock theory presents 14 governing equations which belong to the flow area near the triple point, T. Under the assumptions of thermodynamic equilibrium in states (0), (1), (2) and (3); these 14 governing equations have only 18 parameters, namely: p_0, p_1, p_2, p_3, T_0, T_1, T_2, T_3, u_0, u_1 u_2, u_3, ρ_1, ρ_2, ρ_3, θ_1, θ_2 and θ_3 Four of these 18 parameters must be known for solving these equations successfully.

3.2.3 Modifications of the Perfect Inviscid Analytical Approaches

Two and Three Shock theories, which are presented in Sections 3.2.2.1 and 3.2.2.2, are created with simplified assumptions. However, these assumptions are not fully confirmed. The underlying reason for this is that reflection phenomenon in steady flows are influenced by non-ideal effects. The assumptions, which Two and Three Shock theories are using, are basically [9]:

- The flow is steady.
- The discontinuities at the reflection point of the RR and the triple point of the MR are straight. This in turn implies that the flow fields bounded by these discontinuities are uniform.
- The flow obeys the equation of state of a perfect gas ($p = \rho RT$).
- The flow is inviscid ($\mu = 0$).
- The flow is thermally nonconductive ($k = 0$).
- The contact discontinuity at the triple point of the MR is infinitely thin, i.e., it is a slipstream.

Due to discrepancies in these assumptions, they are discussed individually under this section [9].

3.2.3.1 Nonstraight Discontinuities

Experimental observations present that an MR has significant discontinuities. Both the Mach stem and the slipstream have curves contrary to the assumed. These curves can have significant effects nearby the triple point, this topic is still being investigated. If these curves have significant effects, we can consider that some imperfections exist in available calculations.

3.2.3.2 Thermal Conduction Effects

A real gas has a thermal conductivity. Hence this situation leads to heat transfer, an additional mechanism exists, which might affect the flow fields near the reflection point of an RR and the triple point of an SMR. Neither experimental nor analytical sufficient studies of this possible effect exist.

3.2.3.3 Real Gas Effects

When considering the flow fields near the reflection point of an RR, called R, or the triple point T of an MR, it is quite reasonable to assume that the flow is frozen thermodynamically before shock. However, since the flow moves down from the shock ceiling, the internal freedom ratings are warned (as long as the temperatures are sufficiently high), and the flow fields in front of and behind the reflected shock wave are no longer uniform.

CHAPTER 4

DOUBLE MACH REFLECTION

In this chapter, Double Mach Reflection (DMR) will be defined which is the main topic of this thesis. First, the general characterization of DMR will be announced, then the analytical approaches for DMR will be shown. This chapter is based on [3], [9], [10], [11] and [12].

4.1 DMR Character

When a moving incident shock wave encounters a sharp corner, in summary, four different shock wave reflections can occur, depending upon the Mach number of the incident shock wave M_s, the corner wedge angle θ_w and initial thermodynamic state of the gas (i.e., temperature T_0 and pressure P_0), although for a perfect gas this is not required. These four possible shock waves are shown in Figure 4.1.

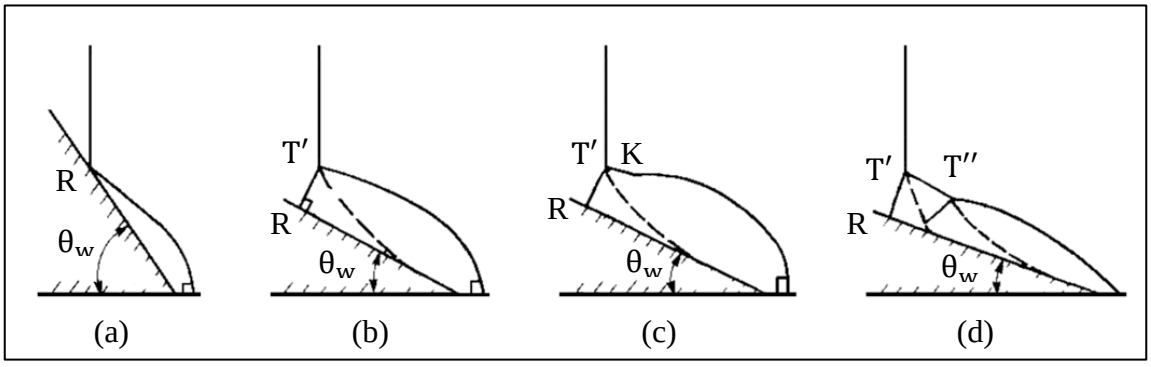


Figure 4.1 Four different shock wave reflections, (a) Regular Reflection (RR), (b) Single Mach Reflection (SMR), (c) Complex Mach Reflection (CMR) and (d) Double Mach Reflection (DMR) [3]

Unlike regular reflection (RR) and single Mach reflection (SMR), which have been well studied and analyzed both experimentally and analytically in literatures, Complex and Double Mach reflections studies are mostly experimental. The possible reason for this

situation is the not sufficiently considered kink point K in CMR and second triple point in DMR until Ben-Dor [3], [11], [12].

Ben-Dor ([3], [9], [11], [12]) had some experimental results from nitrogen gas while studying on the second triple point. Some inconstant oblique shock wave diffractions for imperfect nitrogen gas are seen in Figure 4.2. There are two different diffraction types for DMR between $1 < M_s < 10$. One of them is the shock wave starting to make reflections before the corner, which is described as detached; and the other one is attached.

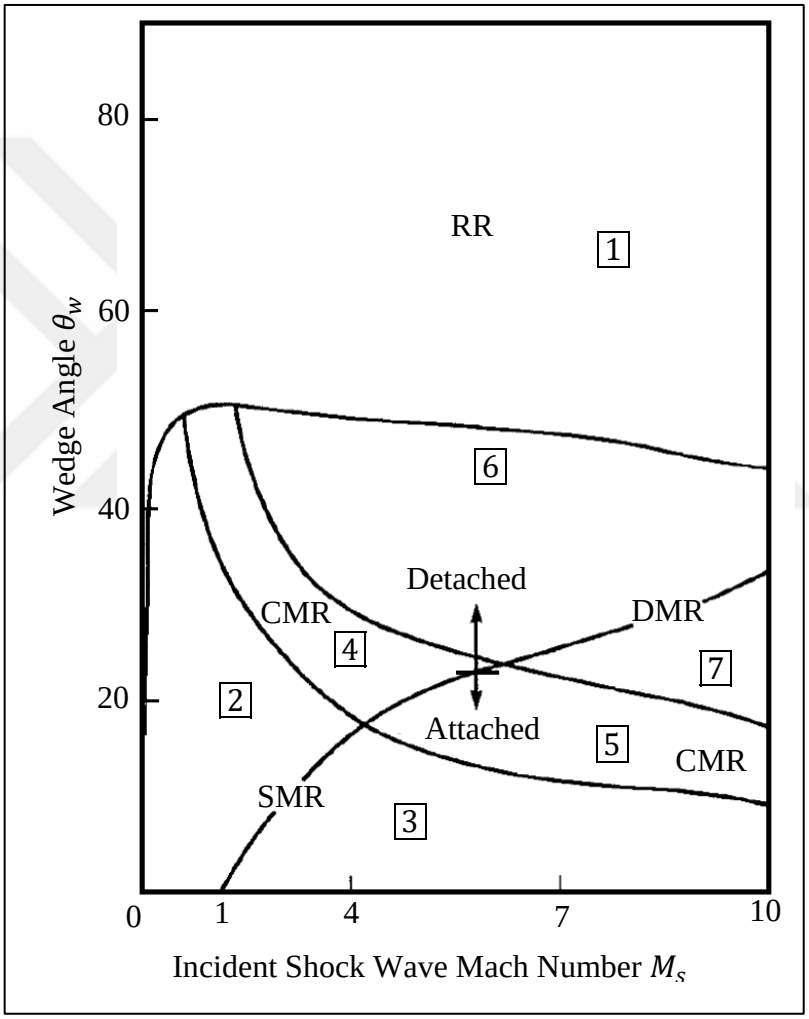


Figure 4.2 Domains of different oblique shock wave diffractions in (M_s, θ_w) plane [3]

In Figure 4.2, lines are for imperfect nitrogen with $P_0 = 15\,Torr$ and $T_0 = 300\,K$, respectively;

1 = Detached RR

2 = Detached SMR 3 = Attached SMR

4 = Detached CMR 5 = Attached CMR

6 = Detached DMR 7 = Attached DMR

Double Mach Reflection process includes seven kind of shock wave reflections; incident shock i, reflected shock wave r, Mach stem m, slip line s, second reflected shock wave r', second Mach stem m' and second slip line s'. If the interaction between the shock wave reflection and flow deflection processes is strong, the compression waves converge to form a shock wave which is called r'. This shock wave has an important role for presence of second triple point T''. It forces the reflected shock wave, r, to occur a strong discontinuity and it makes the second triple point occur. As a continuation, a secondary slip stream compliments this second triple point. For understanding better, a detailed DMR character with shock waves, investigation areas and angles is shown in Figure 4.3. In addition angles χ and χ' which are first T' and second T'' triple points moving angles respectively are seen in Figure 4.3 clearly. Each slip stream and shock wave separate the areas and cause new thermodynamic properties between areas.

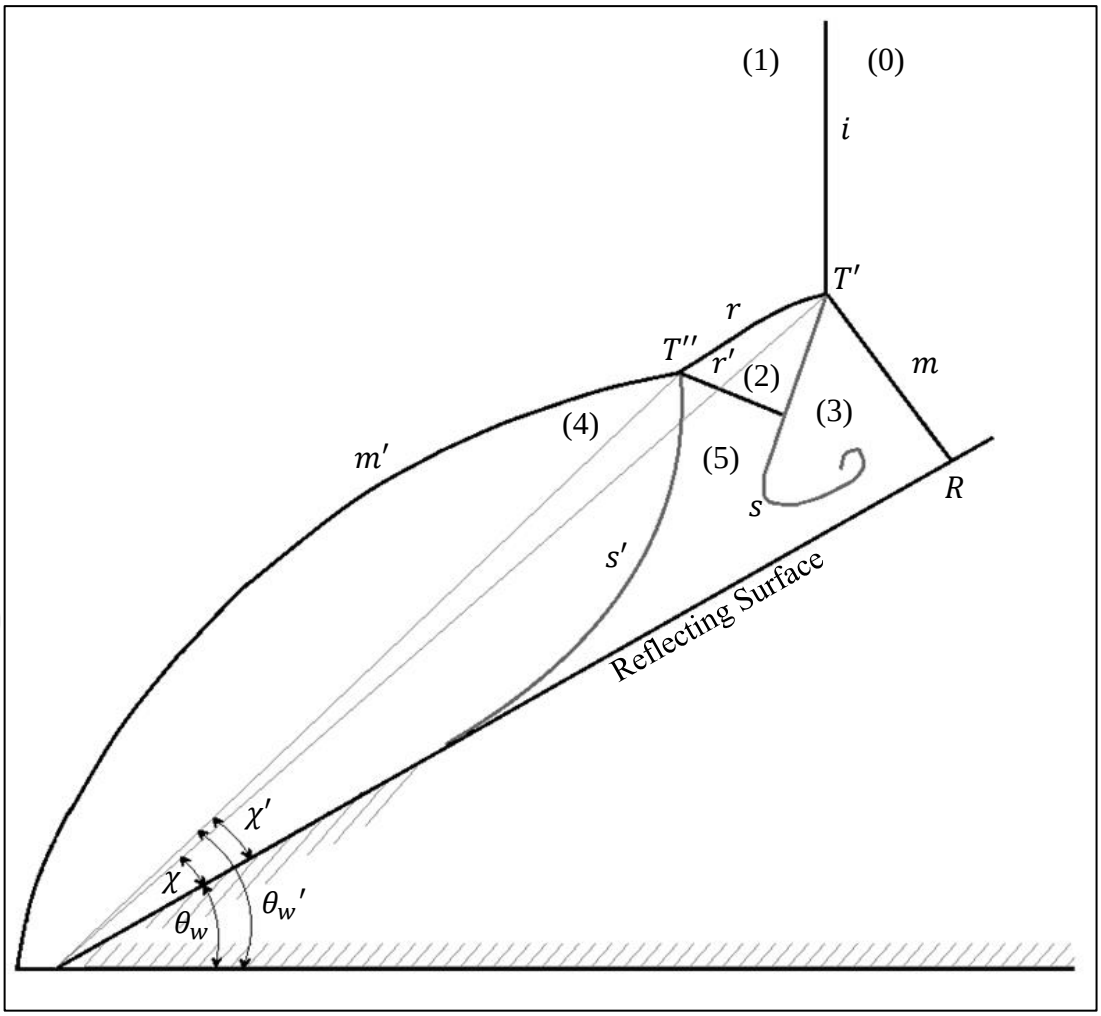


Figure 4.3 Double Mach reflection general characteristic, based on [3]

4.2 Analytical Solutions and Approaches

Previously, researches were carried out on the first triple point. The second triple point is the continuation of these studies and necessarily includes the first triple point equations. Therefore, the second triple point is investigated in this section.

The only way to determine the exact location of the second triple point T'' is solving the entire flow field associated with the DMR. That implies solving the full Navier-Stokes equations. Hence, this task can be done only numerically. In turn, some equations can be obtained with several assumptions as will be shown subsequently and these equations can help for verifying the numerical results with analytical methods.

Assumptions:

- The wave configuration of a DMR is self-similar. (1)
- The gas is an ideal fluid
  ($dinamic\ viscosity\ \mu = 0, hermal\ conductivity\ k = 0$). (2)
- The gas behaves as a perfect gas. (3)
- Mach stem is straight and perpendicular to reflecting surface. (4)
- The second reflected shock wave r' is straight. (5)

The equations for DMR are based on Three-Shock Theory (3ST) for an inviscid flow as mentioned before in Section 3.2.2.2. Subsequently the following equations from 3ST shall be used to verify the simulations.

As we know, there are many unknowns in these equations and they need to be defined. Some of these unknowns, for example ϕ_3, has first triple point angle in its definition for strong waves. In order to be able to continue analytical explanations, firstly DMR with lower Mach numbers (for weak shocks) is shown in Figure 4.4 and with higher Mach number (strong shocks) is shown in Figure 4.5 (a). Strong shock approaches are based on [10].

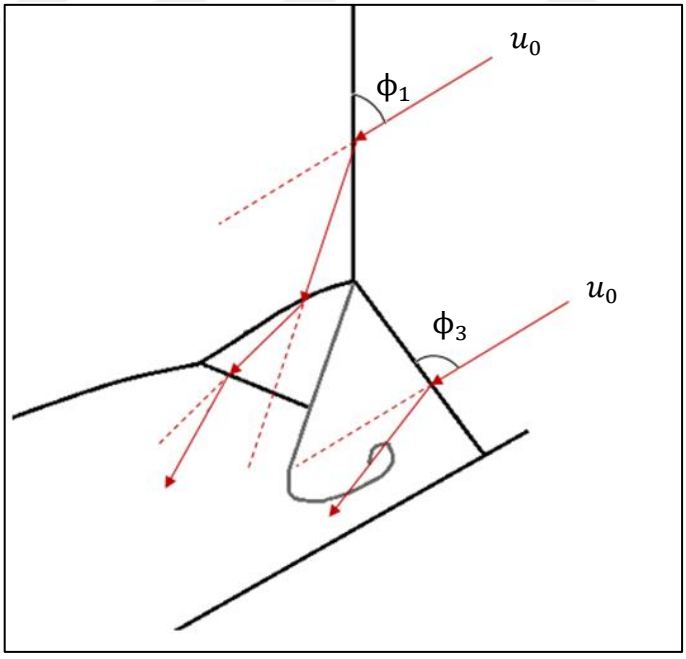


Figure 4.4 DMR characteristic for Ben-Dor approach, based on [9]

For Ben-Dor approach, flow lines are parallel to reflecting surface. The most important differences are about ϕ_1 and ϕ_3.

- Ben-Dor approach:

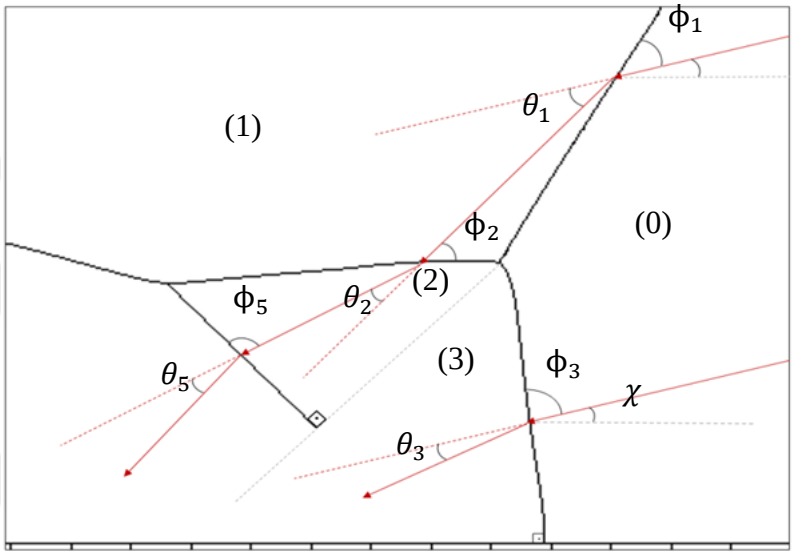
$$\phi_1 = \frac{\pi}{2} - \theta_w \tag{4.1}$$

$$\phi_3 = \frac{\pi}{2} \tag{4.2}$$

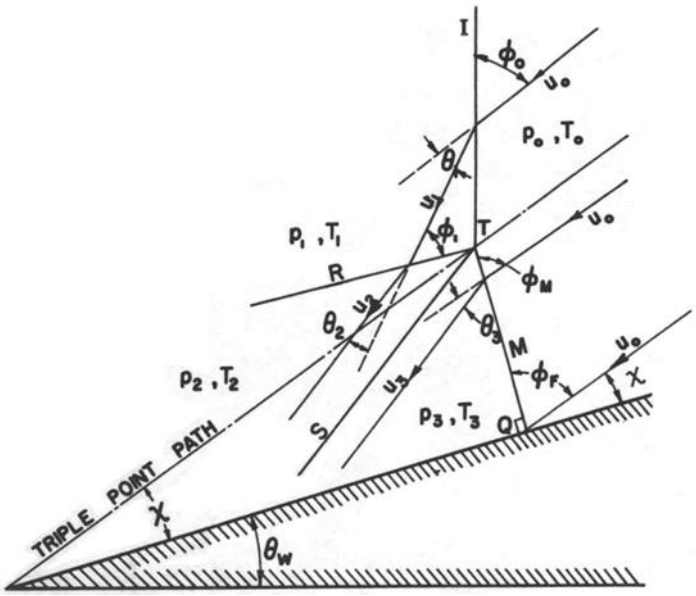
- Law-Glass approach:

$$\phi_1 = \frac{\pi}{2} - (\theta_w + \chi), \quad \phi_3 = \frac{\pi}{2} - \chi \tag{4.3}$$

$$\phi_3 = \frac{\pi}{2} - \chi \tag{4.4}$$



(a)



(b)

Figure 4.5 DMR characteristic for Law-Glass approach (a) simplified schema and (b) Law Glass DMR schema [10]

Due to using $M_s = 10$ in this thesis, wherein the subject is strong wave and as a result of assumption number 4, the Law-Glass approach [10] is used for this thesis.

$$\phi_1 = \frac{\pi}{2} - (\theta_w + \chi) \tag{4.3}$$

$$\phi_3 = \frac{\pi}{2} - \chi \tag{4.4}$$

The final equations for the first and second triple points' angles are taken from references [3], [9] and [10] and are given below.

$$\frac{sin(\chi' - \chi)}{sin(\phi_2 + \chi' - \chi - \theta_1)} = \frac{sin(\chi)}{cos(\phi_3 - \theta_3)} \tag{4.5}$$

$$M_0 = \frac{M_s}{\cos(\theta_w + \chi)} = \frac{M_s}{sin(\phi_1)} \tag{4.6}$$

$$\chi' = 90° - \theta_w - \phi_1{}' \tag{4.7}$$

$$\chi' = 90° - \theta_w - \left(tan\left(\frac{\left(1 - \frac{\rho_0}{\rho_1}\right)}{cot(\phi_1) - \left(\frac{\rho_0}{\rho_1}\right) * cot(\phi_2 - \phi_1 - \theta_1)} \right) \right)^{-1} \tag{4.8}$$

CHAPTER 5

SIMULATIONS

In this chapter, the study which is done will be explained with details and the article [1] which is reference to this thesis will be mentioned. The process of this chapter is respectively; explaining the article [1] briefly, explaining the steps of this study, presenting problems of simulations which were occurred, compare all simulations with each other and analytical solutions with results. For simulations, all values are unitless.

5.1 Summary of Reference Article

The article which is the reference of this thesis for all simulations is named "An immersed boundary solver for inviscid compressible flows". Liu and Hu [1] have investigated a simple and efficient immersed boundary method (IBM) developing for the numerical simulation of inviscid compressible Euler equations. In this article, the dynamic blocked structured adaptive mesh is used to enhance the computational efficiency. In addition, the parallel computation with loading balance is applied by them to save the computational cost for 3D problems but 3D problems were not studied in this thesis. Their Double Mach reflection results from IBM simulations are almost identical solution as that of the boundary-fitted method [1].

Table 5.1 Convergence rate of entropy for adaptive mesh [1]

	Global Error		Local Error	
Grid Level	L_2 Error	Order	L_∞ Error	Order
Level 3-6	1.0253×10^{-4}	-	3.3063×10^{-4}	-
Level 3-7	2.6562×10^{-5}	1.96	9.6194×10^{-5}	1.85
Level 3-8	6.6076×10^{-6}	2.00	2.5607×10^{-5}	1.94
Level 3-9	1.7956×10^{-6}	1.92	8.9556×10^{-6}	1.68

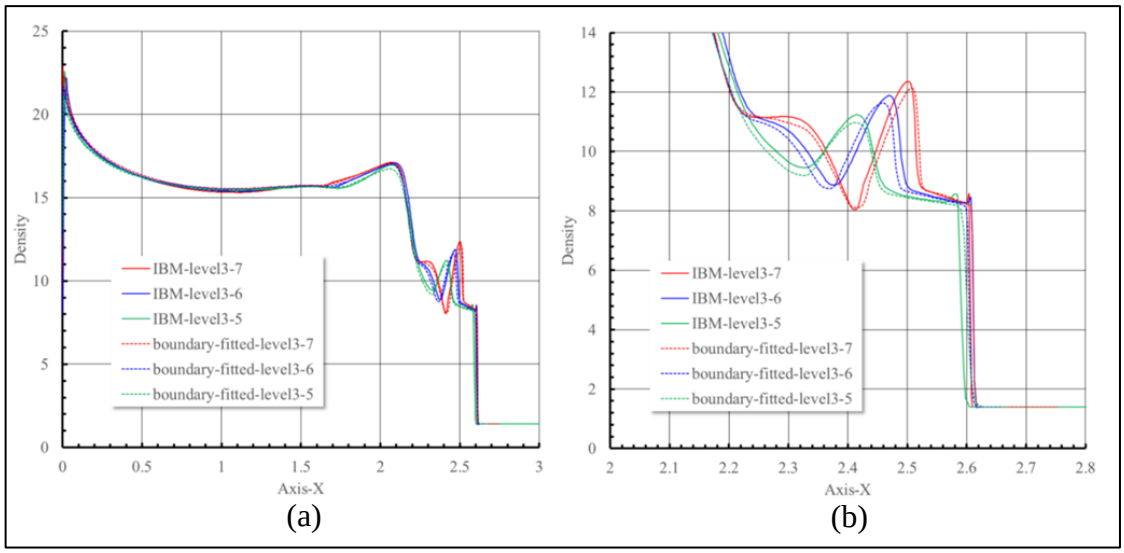


Figure 5.1 Density curves from reference article; (a) density curves and (b) zooming at the results [2]

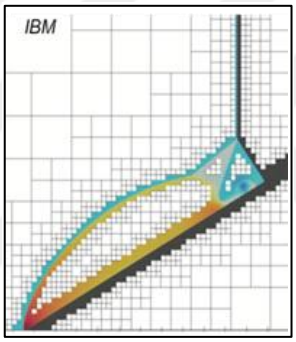


Figure 5.2 Special mesh which the reference article used [1]

Initial conditions are:

$$[\rho_0, u_{0,}\, v_{0,}\, p_0\,] = \begin{cases} [\gamma, 0, 0, 1], & x < (1/6), \\ [8.0, 8.25, 0.0, 116.5\,], & x \geq (1/6) \end{cases}. \qquad (5.1)$$

5.2 Steps of this Study

Under this section, steps of this study are explained and some terms are briefly introduced.

5.2.1 Compressible Navier-Stokes Files

Compressible Navier-Stokes (CNS) files were using for defining the simulations with details. In Appendix-A, one of the CNS files can be seen as pictures. The procedure of

changings on CNS, for having many simulations and using for High Performance Computing (HPC) system, is explained detailed in Appendix-A

5.2.2 High Performance Computing

High Performance Computing (HPC) is a general name of the process which has the meaning of many computers are working for a same problem at the same time. HPC presents very high processing power and an uninterrupted infrastructure.

5.2.3 Bounded Support Spectral Solver

BoSSS (Bounded Support Spectral Solver) is a flexible framework for the development, evaluation and application of numerical discretization schemes based on the Discontinuous Galerkin (DG) method [7]. BoSSS is using the programming language C#. The reason to use that language is, it combines C or C++ with Python which is easy to use. BoSSS has been developed in 2008 at the Chair of Fluid Dynamics, TU Darmstadt [7]. The purpose of BoSSS is serving a research code.

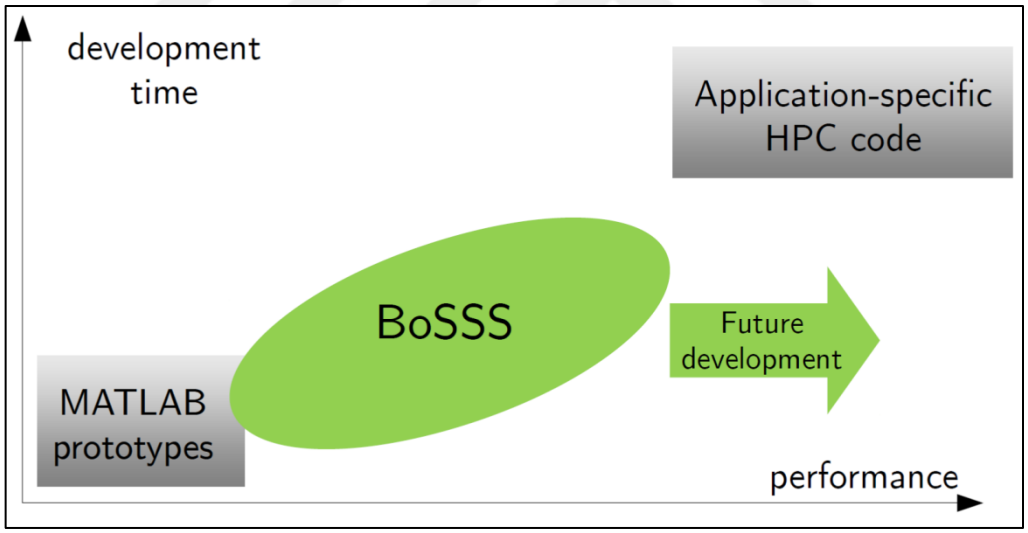


Figure 5.3 BoSSS [7]

BoSSS is more difficult than Matlab but it offers higher performance even though not more than the specific HPC codes.

5.2.4 VisIt

VisIt is a program which can use the plot files of simulations. The simulations can be investigated with almost every detail with this program. Three different plotting options

from VisIt are used for this thesis: Pseudocolor, Curves and Contour which are shown as examples in Figure 5.4. These three options were used for investigating pressure and density values.

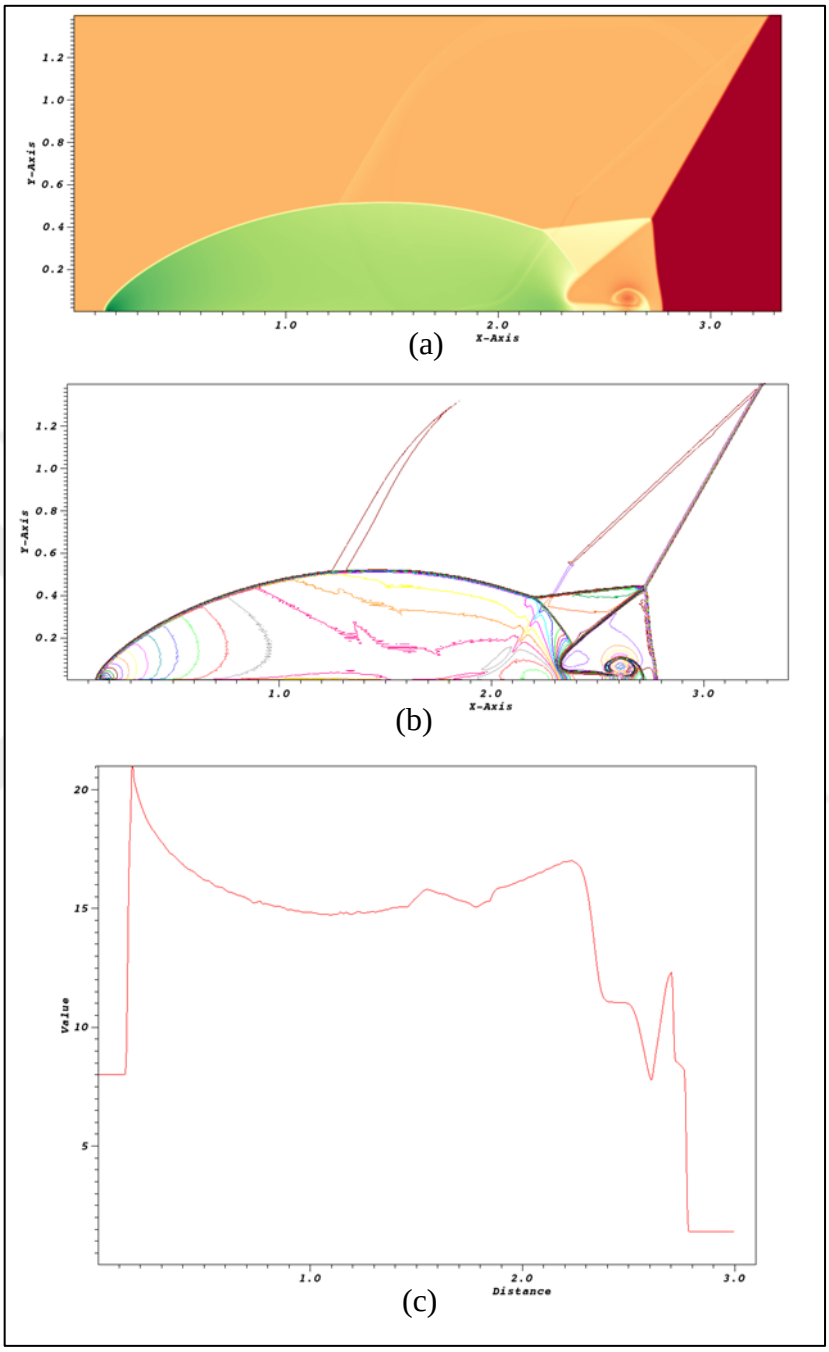


Figure 5.4 VisIt examples for plot options with ρ values for simulation 800x280 grid cells at 0.20 end time for 3rd DG degree: (a) Pseudocolor, (b) Contour, (c) Curve

5.2.5 Engauge Digitizer

Engauge Digitizer is a program which is able to define its own coordinates and values. A picture of a graphic can be copied to that program, after defining coordinates, values

can be marked by user. In the end, this program can give the values of marked points depended on defined coordinates. For this thesis, these numbers could be copied to Excel program and then plot again for comparing with other simulations.

5.2.6 Summary of the Process

The process which is generally followed to reach the results are given below and shown in Figure 5.5.

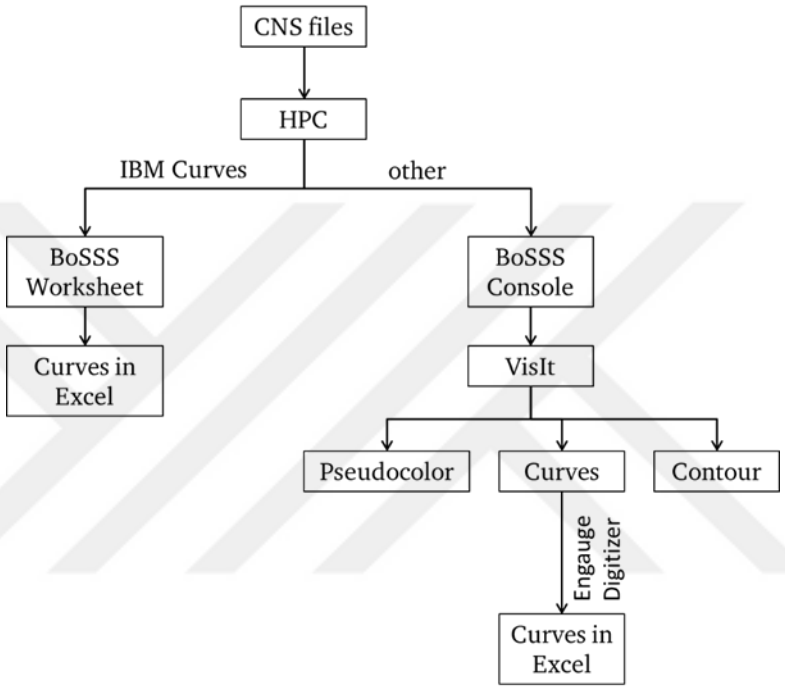


Figure 5.5 Process which is generally followed to reach the results

First, CNS files that give the initial conditions for the solution are changed in the intended values. After that, these CNS files are used in HPC system and the simulations are started on HPC system. The VisIt program is used to illustrate the results which are obtained from HPC. Since the format of the HPC results is not suitable for VisIt, the BoSSS Console program is used to convert the results to a ".plot" file. The plots which are seen in this thesis are obtained with ".plot" files which are obtained from BoSSS Console.

Simulations in 0^{th} DG degree have not enough data from HPC results, hence the parameters are not enough for using the Contour option. Besides, IBM simulations which have ramp in their solution could not be plotted clearly on reflecting surface with 30°. Instead of VisIt, BoSSS Worksheet was used for plotting curves of IBM simulations.

As will be seen as the difference between curves in Figure 5.3 (a) and Figure 5.1 which is in Section 5.1, curves results are converted with program “Engauge Digitizer” for using in Excel. With “Engauge Digitizer”, a coordinate system can be defined on a reference picture and in this coordinate system, the values on the reference picture can be defined. The values which are defined can be saved as an Excel file. In this thesis, curve plots were used from Excel files. In addition, the curve plots from reference article [1] were obtained with Engauge Digitizer either.

5.3 Introduction for Simulations

Fifteen simulations including four IBM were conducted. In addition, five of these fifteen simulations end times are 0.20, the rests’ end times are 0.25. The reason of these diversities are:

- End Time 0.25 : Most of the literatures are studied at end time 0.25.
- End Time 0.20 : Liu and Hu [1] used the end time 0.20.

Every simulation has an end time in their own CNS file. End time is decided by determining the optimum number of times to achieve reasonable results.

Initial conditions are the same with reference article [1]. List of simulations are given in Table 5.2 and three examples of simulations with their names are given in Figure 5.6.

Table 5.2 BFM Simulations

BFM		0.20 End Time		0.25 End Time
0th DG Degree		2048x512 Grid Cells		800x200 Grid Cells
0th DG Degree				1200x300 Grid Cells
0th DG Degree				1200x420 Grid Cells
0th DG Degree				2400x600 Grid Cells
1st DG Degree		800x280 Grid Cells		800x200 Grid Cells
2nd DG Degree				800x200 Grid Cells
3rd DG Degree		800x280 Grid Cells		400x100 Grid Cells
3rd DG Degree				400x140 Grid Cells

Table 5.3 IBM Simulations

IBM		0.20 End Time		0.25 End Time
0th DG Degree		600x420 Grid Cells		600x240 Grid Cells
0th DG Degree		1024x1024 Grid Cells		600x525 Grid Cells
2nd DG Degree		300x300 Grid Cells		

Simulation 300x300 grid cells at 0.20 end time for 2nd DG degree (IBM) could not finished because of some problems on HPC and long time solving.

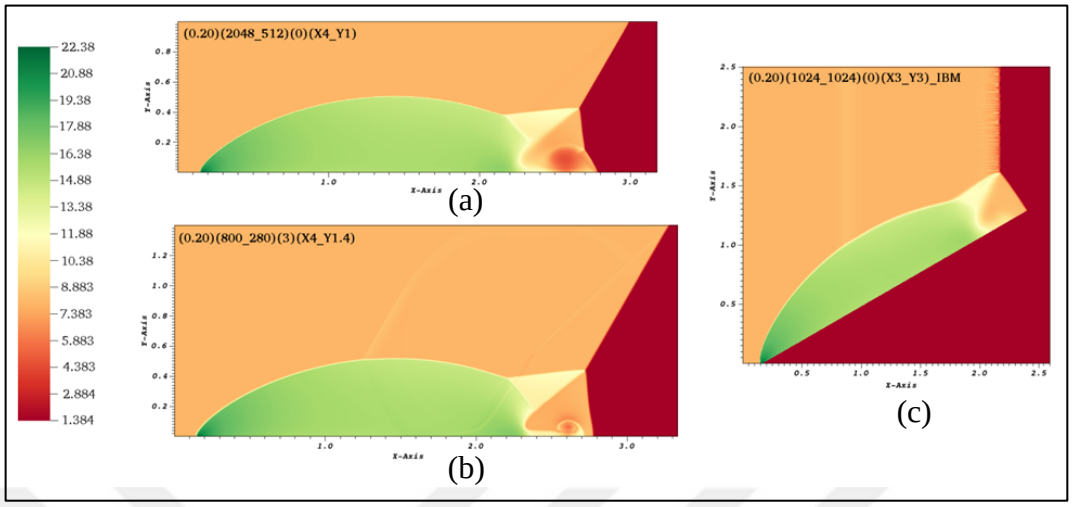


Figure 5.6 Several simulations which were resolved: (a) Finest grid cells for 0.20 end time, (b) Finest grid cells for 3rd DG degree, (c) Finest grid cells among IBM simulations

5.4 Problems of Simulations

While simulations are performed, some problems are encountered. In this section, these problems are explained and illuminated.

5.4.1 Kink on Mach Stem

One of the possible reasons of the kink which is shown in Figure 5.7 is insufficient parameters because of 0th DG degree for solving these simulations. The mentioned kink is not observed in the simulations with higher DG degrees. The other possible cause could be about the solution method because the kink, which is mentioned, was not observed for IBM simulations.

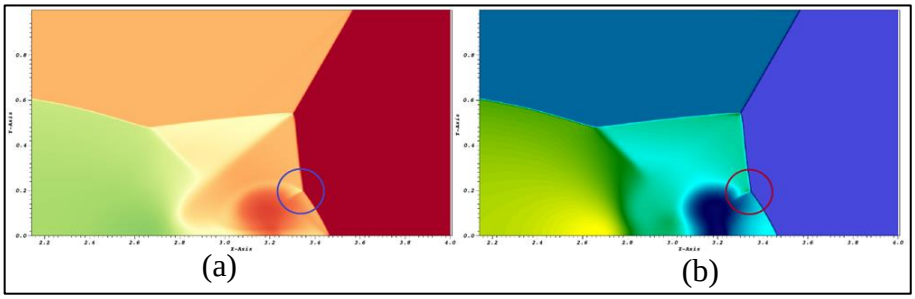


Figure 5.7 The Kink which appears on Mach stem on the simulation 800x200 grid cells at 0.25 end time for 0th DG degree, values for (a) Density, (b) Pressure

On Mach stem, there is an unexpected kink as seen as all boundary fitted simulations for 0^{th} DG degree. That kink is shown closely in Figure 5.7 for simulation 2400x600 grid cells at 0.25 end time for 0^{th} DG degree.

5.4.2 Recirculation in Area (3)

Instead of problem, it would be more appropriate to say that recirculation not described yet, but still subject to be investigated. The recirculation, which is shown in Figure 5.8, is not related to grid cells, DG degrees or calculation method; but is caused by DMR shock waves.

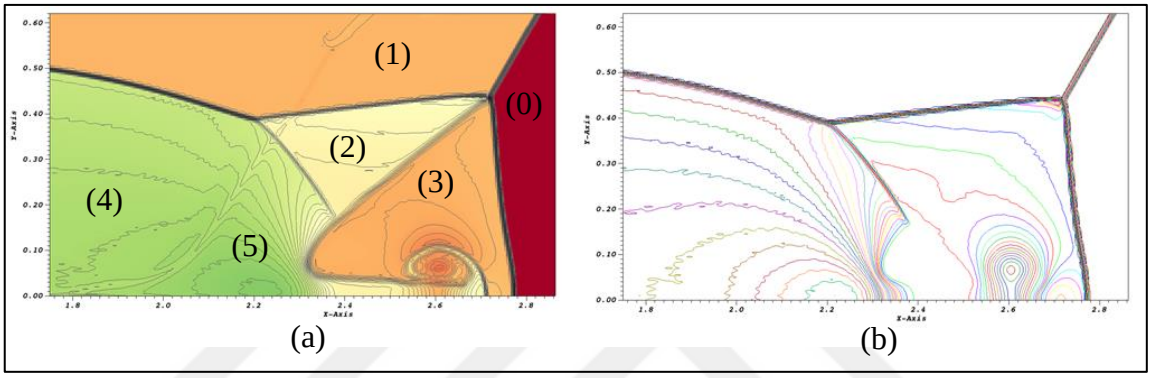


Figure 5.8 Detailed plot from the area (3) for 800x280 at 0.20 end time and 3^{rd} DG degree, values for (a) Density, (b) Pressure

For the simulations which have 0.25 end time, recirculation is observed $x \in [2.5, 3.5]$ as seen in Figure 5.8. 800x280 grid cells at 0.20 end time for 3^{rd} DG degree is chosen for showing this situation due to easier to observe the recirculation with high DG degrees and high grid cells. In addition, the recirculation can be observed clearly in all curve figures on $x \in [2.5, 3.5]$ and as an example one of them is shown in Figure 5.9.

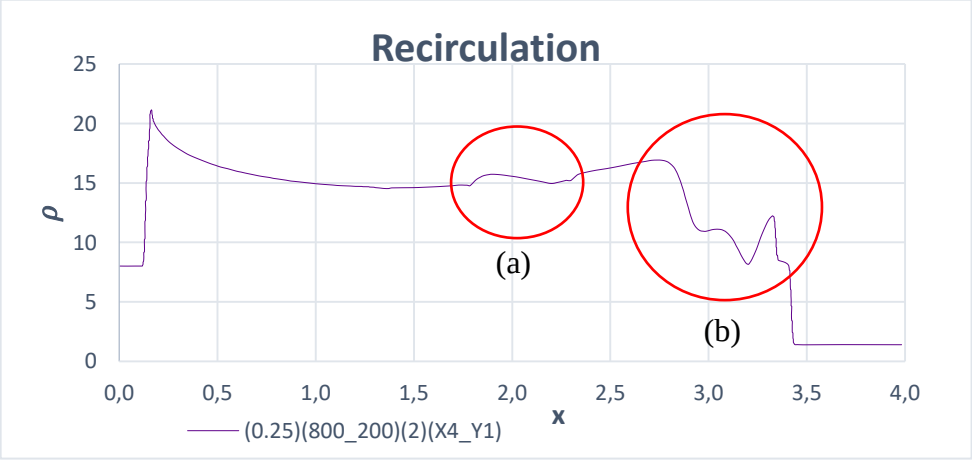


Figure 5.9 Recirculation (a) between area (4)-(5) and (b) recirculation in area (3)

The possible reason of the recirculation, which are shown in also Figure 5.9 (a) and (b), can be about slip line and secondary slip line, respectively.

5.4.3 Irregularity on Incident Shock Wave from IBM Simulations

As seen as in Figure 5.10, there is an irregularity at the top of incident shock wave. For this reason, simulation which has higher maximum Y value was performed. It has been observed that the same irregularity in the simulation with higher Y is still at the top. It implies that changing maximum Y does not affect that irregularity on incident shock wave.

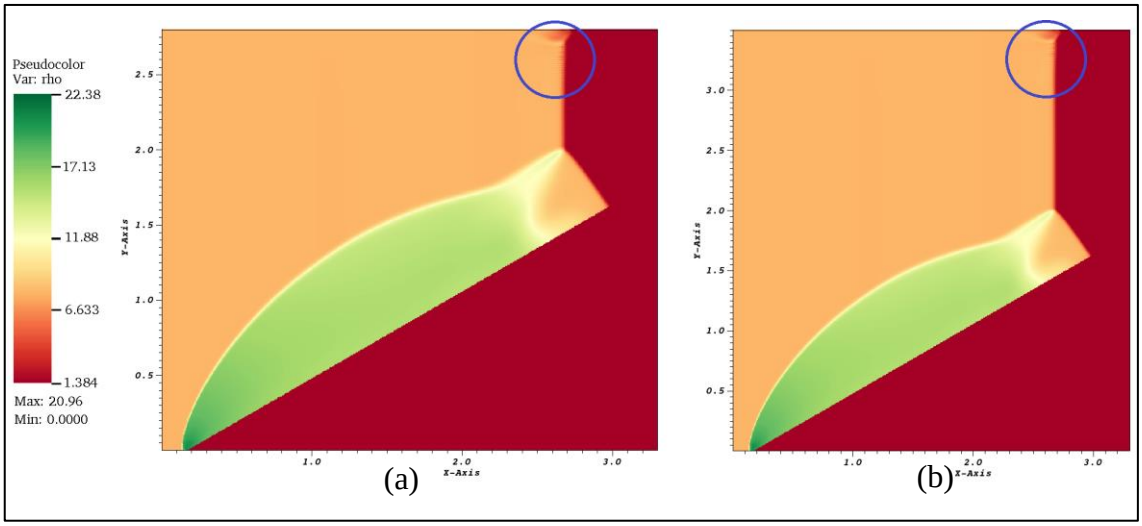


Figure 5.10 Irregularity on incident shock wave (a) 600x420 grid cells at 0.25 end time for 0^{th} DG degree (IBM) and (b) 600x525 grid cells at 0.25 end time for 0^{th} DG degree (IBM)

The possible reason for this problem can be grids because of the immersed boundary method. In any case, the density and pressure values are reasonable and the same with each other in every area. In addition, these values are very close to the other values of other simulations. It implies that this irregularity does not affect the values.

5.4.4 Trace of Incident Shock Wave

Some density and pressure fluctuations, which are shown in Figure 5.11 (a) and (b), respectively, are observed in area (1) in simulations which are performed with high DG degrees or high grids.

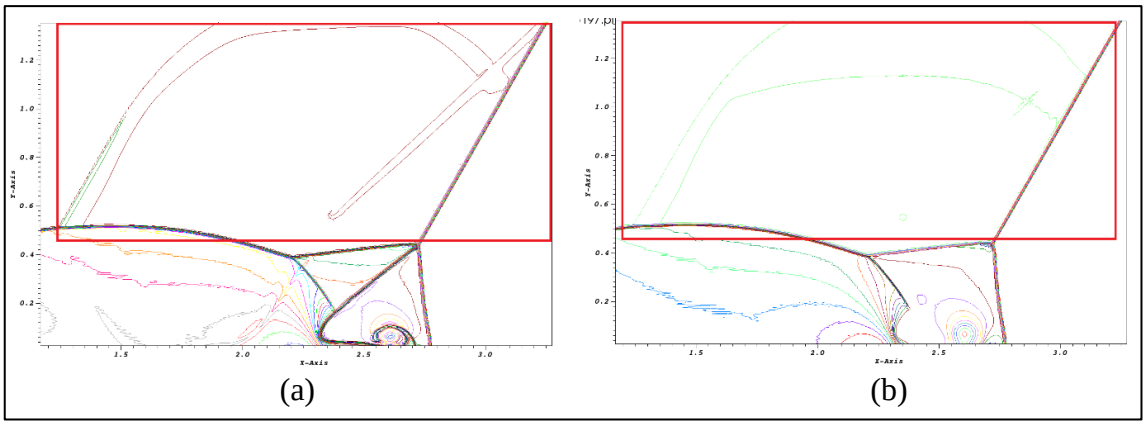


Figure 5.11 Fluctuations on incident shock wave on simulation 800x280 grid cells at 0.20 end time for 3rd DG degree (a) for density and (b) for pressure

These fluctuations began to be observed from the moment of the formation of the shock wave also for IBM simulations. In Figure 5.12 (a) and (b), the mentioned trace is observed on BFM and IBM simulations on pseudocolor, respectively.

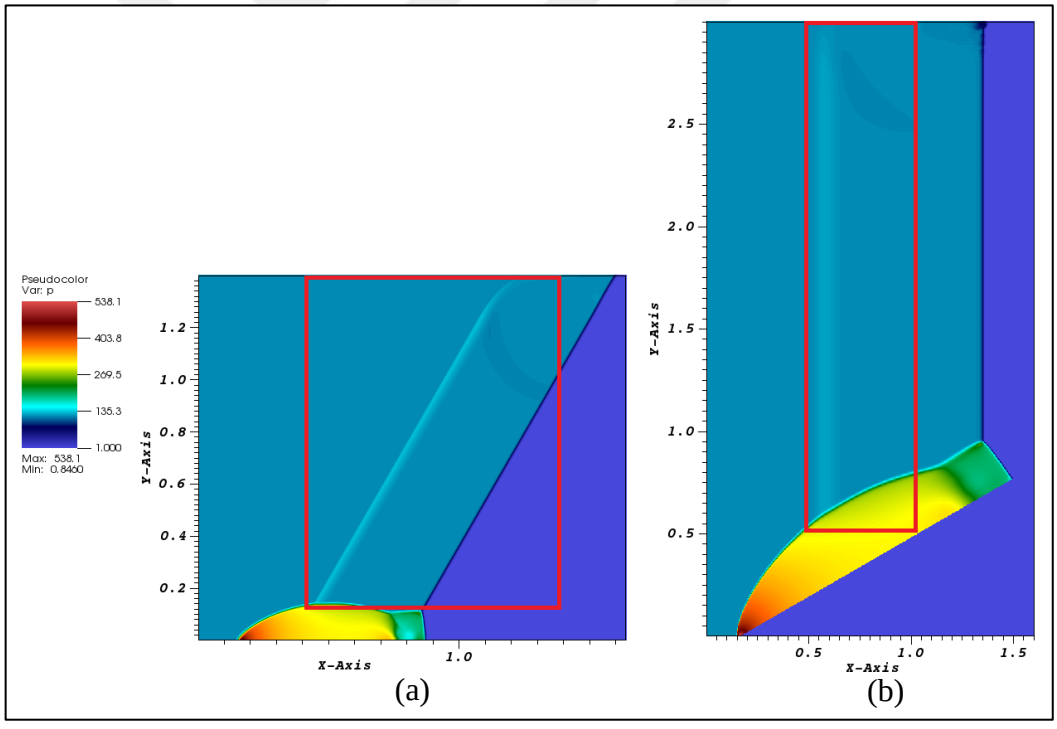


Figure 5.12 Fluctuations on incident shock wave at half time steps on simulations (a) 800x280 grid cells at 0.20 end time for 3rd DG degree and (b) 1024x1024 grid cells at 0.20 end time for 0th DG degree (IBM) for pressure

A solution has not been found for this fluctuation which is observed more noticeable in high-resolution simulations and less noticeable in low resolution simulations

5.5 Comparison

The differences between simulations are shown under this section with mostly ρ curves of simulations on y=0 and x ∈ [0, 4] or x ∈ [0, 3]. Further that, ρ and p pseudocolor plots are used for explaining some differences clearly.

5.5.1 Effect of Maximum Y Height

The reason for the drawn attention to this topic is an irregularity on incident shock wave as shown in Figure 5.13. It was observed in Section 5.4.3 that the different maximum Y high do not affect the results. Nevertheless, to provide more, ρ during the surface is investigated for simulations 400x100 grid cells at 0.25 end time for 3rd DG degree and 400x100 grid cells at 0.25 end time for 3rd DG degree and it is proved that they are the same as each other.

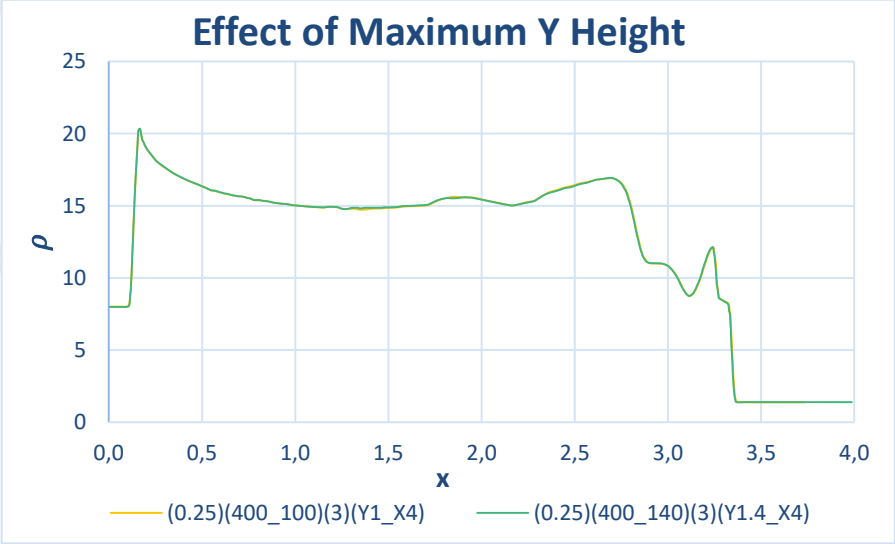


Figure 5.13 Effect of maximum Y height for 400x100 grid cells at 0.25 end time for 3rd DG degree and 400x140 grid cells at 0.25 end time for 3rd DG degree

5.5.2 Grid Comparison

The simulations started performing with 800x200 grid cells at 0.25 end time for 0th DG degree which has the coarsest grid cells among 0th DG degrees in boundary fitted method and additionally simulations with higher grid cells are tried in order to reach better results. Under this section, coarsest and finest grid cells for BFM and IBM are investigated. In addition, Figure 5.12 which is containing BFM simulations for 0.25 end time with 0th DG degree can be found.

5.5.2.1 Coarsest and Finest Grid Cells

In Figure 5.14, simulations which have coarsest and finest grid cells are shown and compared. Simulation 800x200 grid cells at 0.25 end time for 0^{th} DG degree which is shown in Figure 5.14 (a) has the coarsest grid cells among 0^{th} DG degrees for BFM. This simulation is the first simulation which was performed. The main reason was trying to get meaningful results from simulations. Simulation 2400x600 grid cells at 0.25 end time for 0^{th} DG degree which is shown in Figure 5.14 (b) has the finest grid cells among all simulations. The reason of resolving this simulation is trying to get best results in the frame of at 0.25 end times for 0^{th} DG degrees.

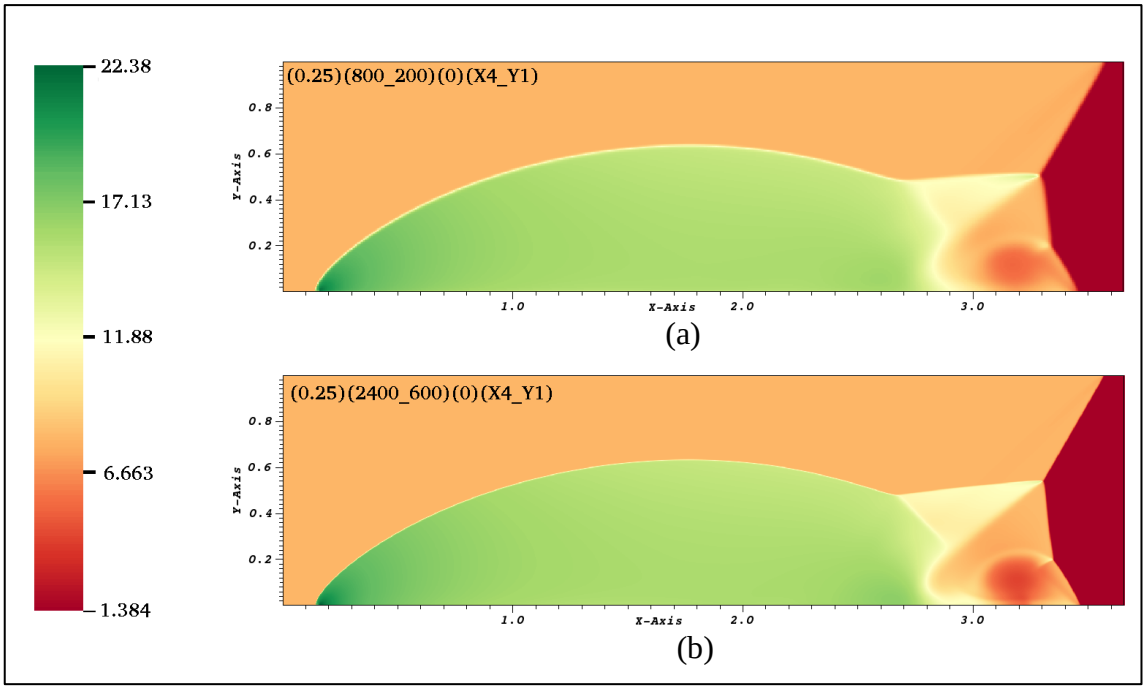


Figure 5.14 The coarsest and the finest grid cells for 0^{th} DG degree, (a) 800x200 grid cells at 0.25 end time for 0^{th} DG degree, (b) 2400x600 grid cells at 0.25 end time for 0^{th} DG degree

It is observed that using higher grid cells in simulation analysis provides more effective results. In Figure 5.14 (b), the detailed plot and sharp borders can be seen more clearly than in Figure 5.14 (a). The kink problem, which was mentioned, and the area (3), which has most mixed values, can be seen in Figure 5.14 (b) clearly.

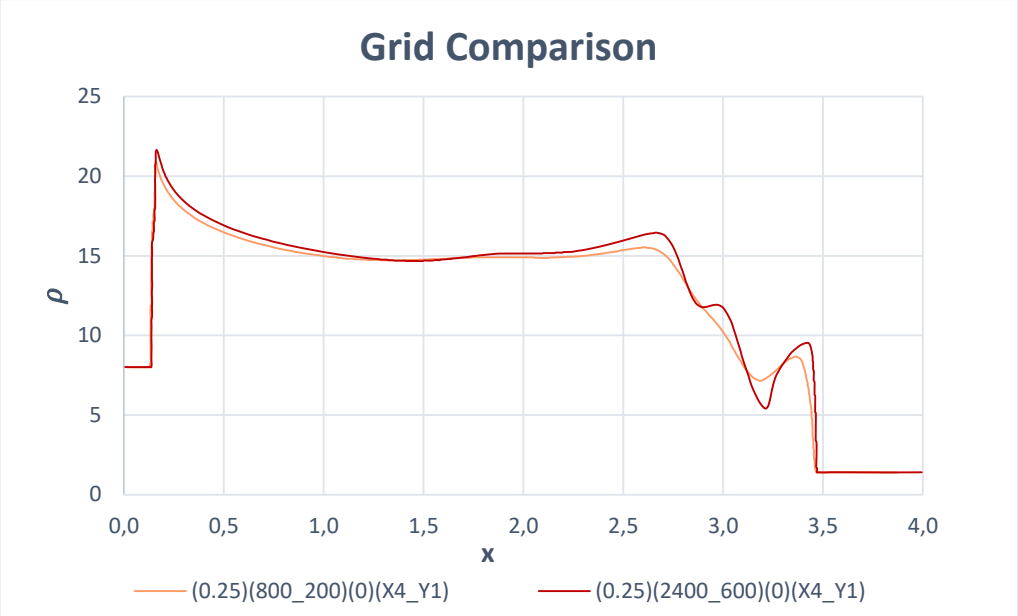


Figure 5.15 The coarsest and the finest grid cells comparison for BFM, 0.25 end time with 0^{th} DG degree

The main goal of comparing 600x420 grid cells at 0.20 end time for 0^{th} DG degree (IBM) and 1024x1024 grid cells at 0.20 end time for 0^{th} DG degree (IBM) simulations, which are shown in Figure 5.16, is seeing how the grid cell numbers affect to results of IBM simulations.

Due to the complexities in $x \in [2.5, 3.5]$, there are irregularities in Figure 5.15 and Figure 5.16. Moreover, it is more obvious for simulation 2400x600 grid cells at 0.25 end time for 0^{th} DG degree and 1024x1024 grid cells at 0.20 end time for 0^{th} DG degree (IBM) because of high grid resolution.

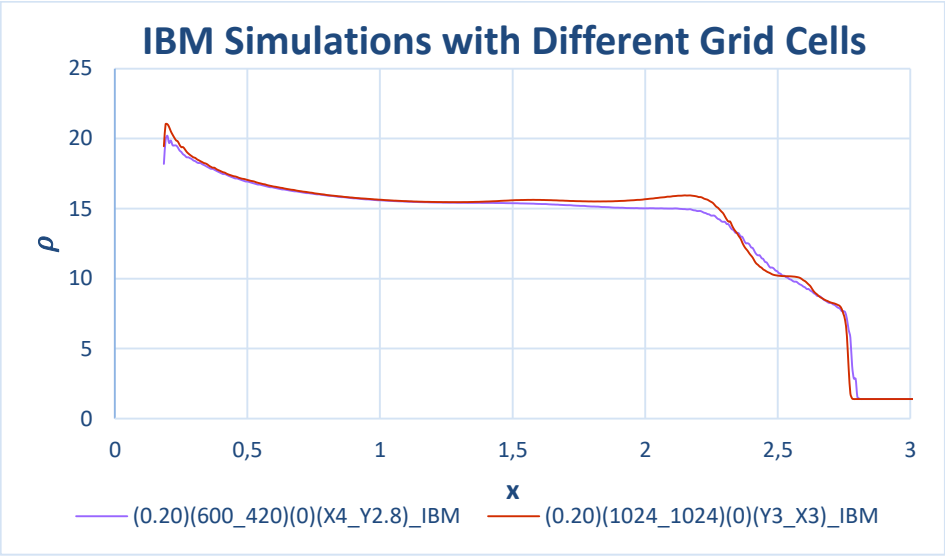


Figure 5.16 The coarsest and the finest grid cells for 0^{th} DG degree (IBM)

5.5.2.2 All 0^{th} DG Degrees: For Boundary Fitted Method for 0.25 End Time with 0^{th} DG Degree

The main goal of comparing all BFM simulations for 0.25 end time for 0^{th} DG degree, which are shown in Figure 5.17, is seeing how much ρ values are close to each other. In simulation 2400x600 grid cells at 0.25 end time for 0^{th} DG degree, which has the highest grids, the complexities in area (3) are observed better.

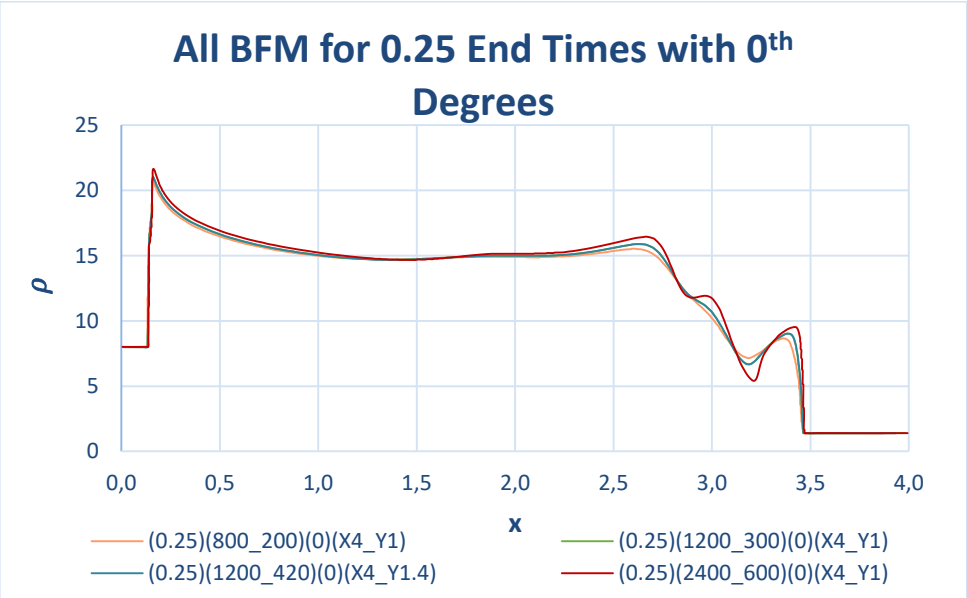


Figure 5.17 All BFM at 0.25 end times for 0^{th} DG degrees

5.5.3 Degree Comparison

The major changes in the results observed are obtained by varying DG degrees. In this section, at 0.25 end times for 0^{th}, 1^{st} and 2^{nd} DG degrees and at 0.20 end times for 1^{st} and 3^{rd} DG degrees are presented.

5.5.3.1 Coarsest and Finest Grid Cells

Simulation 800x280 grid cells at 0.20 end time for 3^{rd} DG degree has the finest grid cells among 3^{rd} DG degrees. The reason of performing this simulation is comparing with the simulation which has the finest grid cells at 0.20 end time for 0^{th} DG degree (2048x512 grid cells at 0.20 end time for 0^{th} DG degree). But it is as well to the most detailed results among all simulations are obtained from simulation 800x280 grid cells at 0.20 end time for 3^{rd} DG degree.

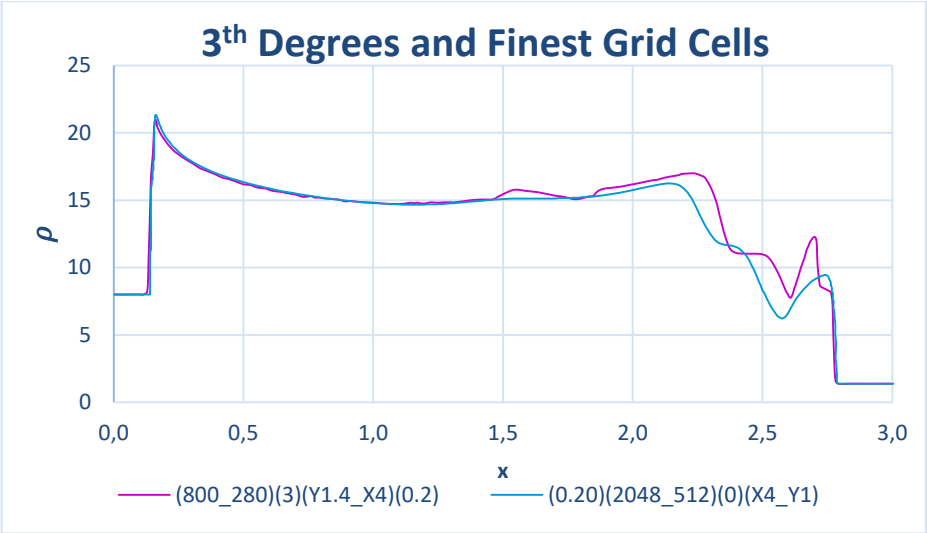


Figure 5.18 3rd DG degrees and finest grid cells comparison with curves

As seen in Figure 5.18, although the results are very close to each other even so the simulations for 3rd DG degree have more accurate results.

5.5.3.2 0th, 1st and 2nd DG Degrees at 0.25 End Time

The main goal of comparing 800x200 grid cells at 0.25 end time for 0th, 1st and 2nd DG degrees simulations are seeing how the DG degrees affect to results.

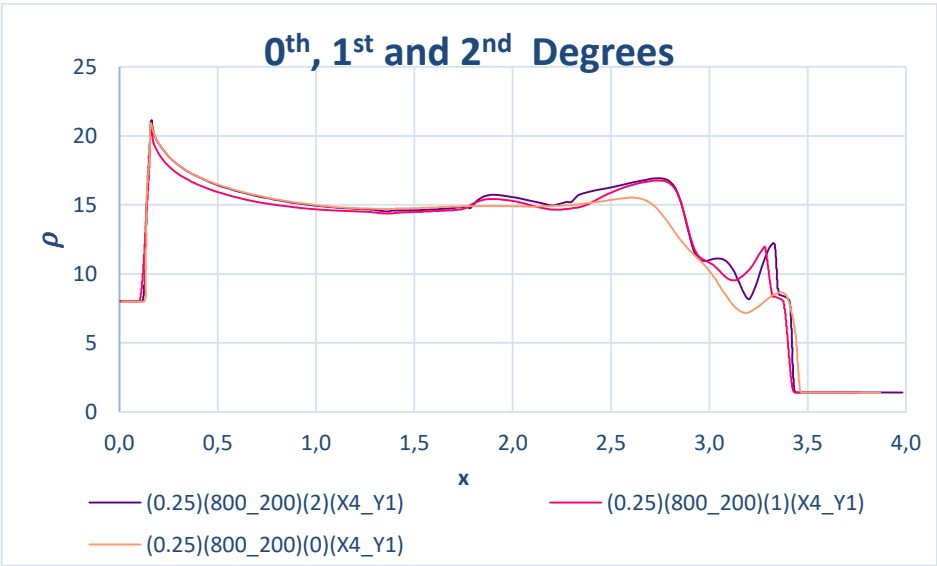


Figure 5.19 0th, 1st and 2nd DG degrees comparison with curves

As seen as Figure 5.19, around x=2, there are complexities for 1st and 2nd DG degrees unlike 0th DG degree. The reason of this difference is about inadequate solution of 0th DG degree. In addition, mobility in x ∈ [2.5, 3.5] can be seen more with 1st and 2nd DG degrees.

5.5.3.3 1st and 3rd DG Degrees at 0.20 End Time

The main goal of comparing 800x280 grid cells at 0.20 end time for 1st and 3rd DG degrees is seeing how the DG degrees affect to results. If the DG degree is increased from the 1st DG degree, it is observed that the results are more similar to each other and presenting more accurate values as seen in Figure 5.20.

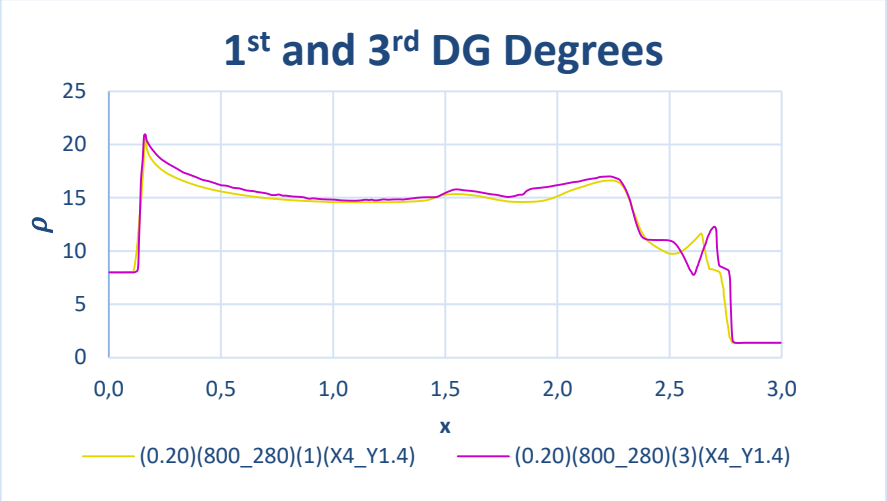


Figure 5.20 1st and 3rd DG degrees at 0.20 end time comparison with curves

5.5.4 Immersed Boundary – Boundary Fitted Methods

Simulation 1024x1024 grid cells at 0.20 end time for 0th DG degree (IBM) has the finest grid cells among IBM simulations and shown in Figure 5.21. The reason of resolving this simulation is trying to get best results from IBM simulations.

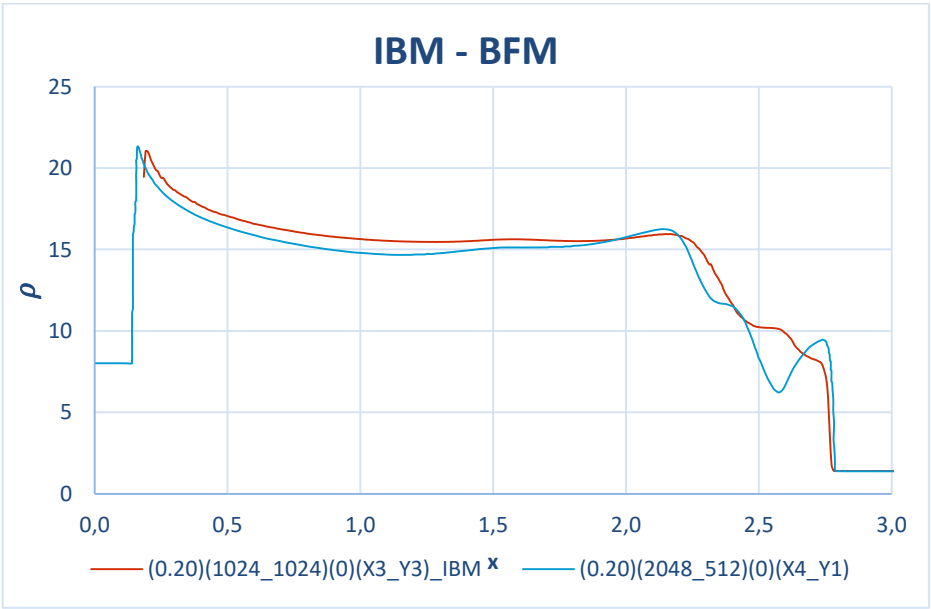


Figure 5.21 Immersed boundary and boundary fitted method comparison with curves

In order to compare results from IBM and BFM, these simulations are plotted as curves with simulation 2048x512 grid cells at 0.20 end time for 0^{th} DG degree in Figure 5.21. On the general observations made, it is concluded that the boundary fitted method gives better results than the immersed boundary method. The immersed boundary method needs higher resolution to yield better results such as the boundary fitted method.

5.5.5 End Time Comparison

The main goal of investigating 800x280 grid cells at 0.20 end time for 1^{st} DG degree and 800x200 grid cells at 0.25 end time for 1^{st} DG degree simulations are seeing how the different end times affect to results.

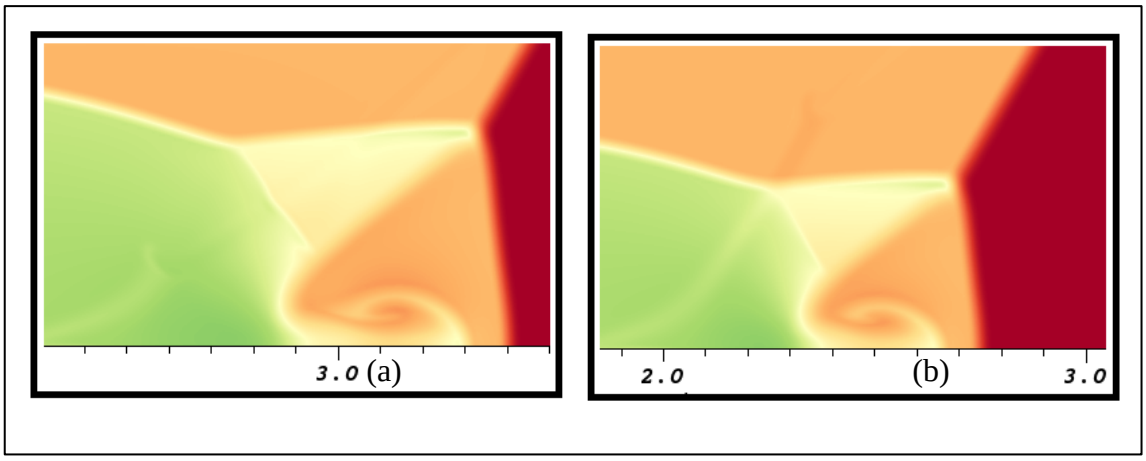


Figure 5.22 End time comparison with pseudocolor for (a) 800x200 grid cells at 0.25 end time for 1^{st} DG degree and (b) 800x280 grid cells at 0.20 end time for 1^{st} DG degree

Although there are not many significant differences, as expected, the difference between these two simulations is that the simulation 800x280 grid cells at 0.20 end time for 1^{st} DG degree is not developed as simulation 800x200 grid cells at 0.25 end time for 1^{st} DG degree. The comparison about the development can be easily seen by looking at the area (3) as shown in Figure 5.22. The values in the results obtained from the regions are also sufficiently close to each other.

5.5.6 Article Comparison

The main goal of investigating 800x280 grid cells at 0.20 end time for 1^{st} DG degree and article simulations is seeing the difference between simulations and reference article [1].

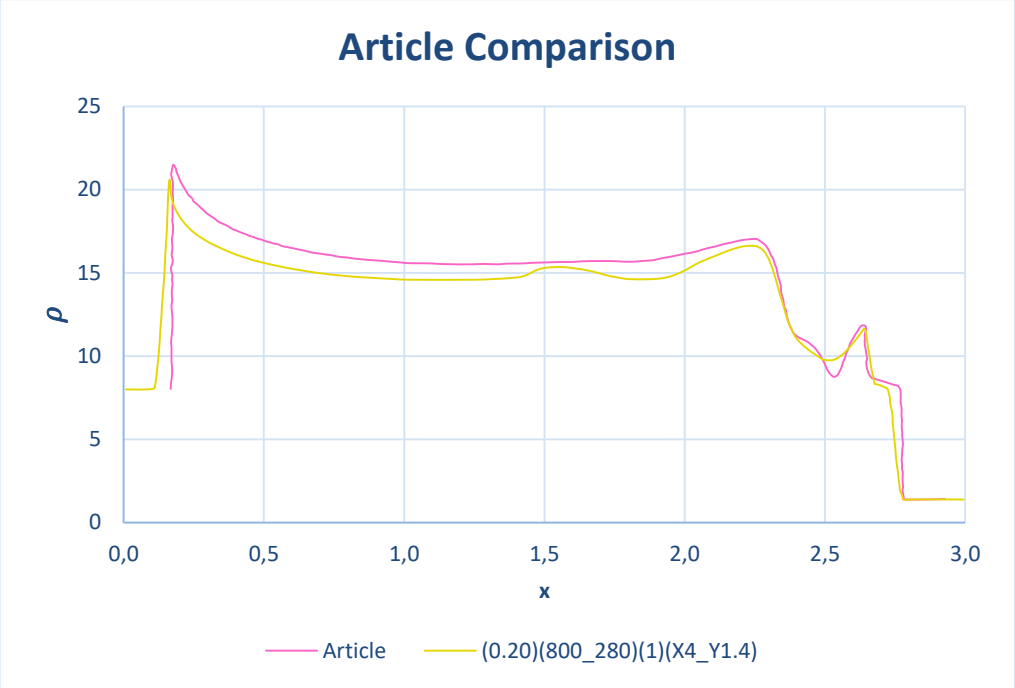


Figure 5.23 Article comparison with curves

As seen in Figure 5.23, especially on x ∈ [2.2, 3.0], a high similarity is observed. One of the reasons for the observed differences is the grid quality difference, the other one can be about inaccuracies while using the program Engauge Digiziter for article plot.

5.6 Analytical Solutions

The simulations which are performed are similar to the simulations in the literatures which are performed up to now. Under this section, the intent of the calculations is verifying the simulations accurately with analytical solutions.

Area separation with ρ, p and u values is shown in Figure 5.24 and all requirements shown in Figure 5.25 closely as if the Figure 5.24 rotated 30° degrees to be fully perceived.

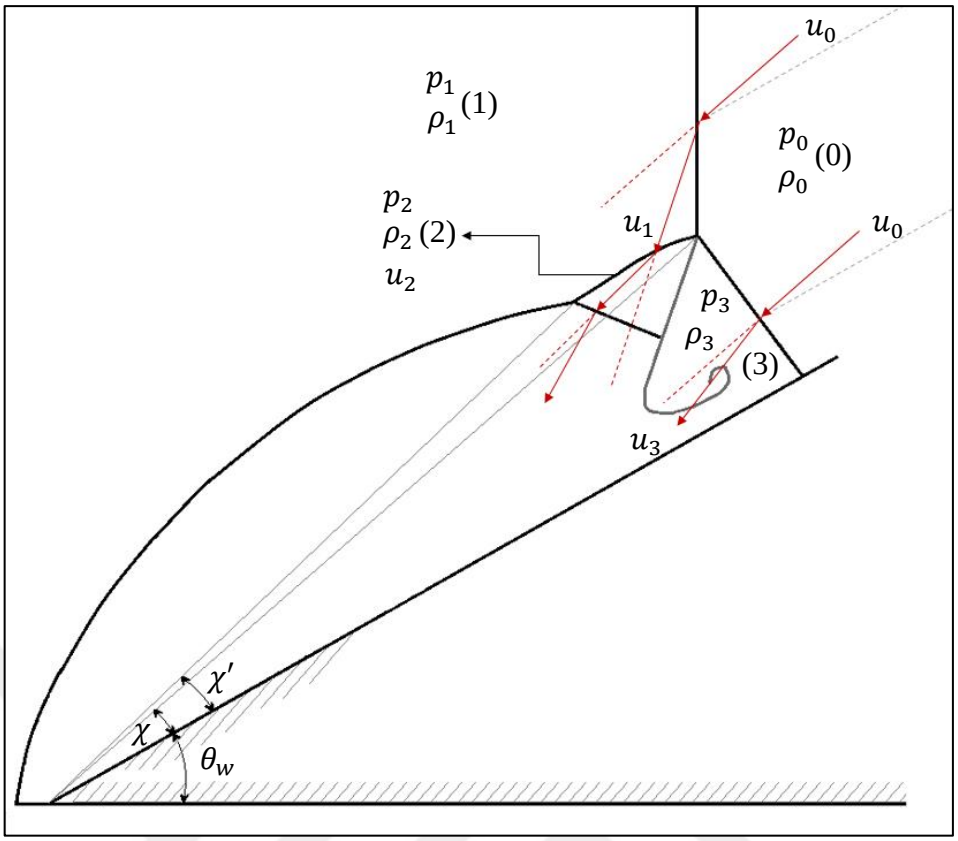


Figure 5.24 Area separation with ρ,p and u values

Knowns are: $\boldsymbol{\gamma = 1.4}$, $\boldsymbol{p_r = 1\,[p_0]}$, $\boldsymbol{\rho_r = \gamma = 1.4\,[\rho_0]}$, $\boldsymbol{M_s = 10}$, $\boldsymbol{\theta_w = 30°}$

Some values from conditions can be found in basic equations of [9].

$$\boldsymbol{V_s} = M_s * \sqrt{\frac{(\gamma * p_r)}{\rho_r}} = \boldsymbol{10} \tag{5.2}$$

$$\boldsymbol{p_1} = \frac{2 * \gamma * {M_s}^2 - (\gamma - 1)}{\gamma + 1} = \boldsymbol{116.5} \tag{5.3}$$

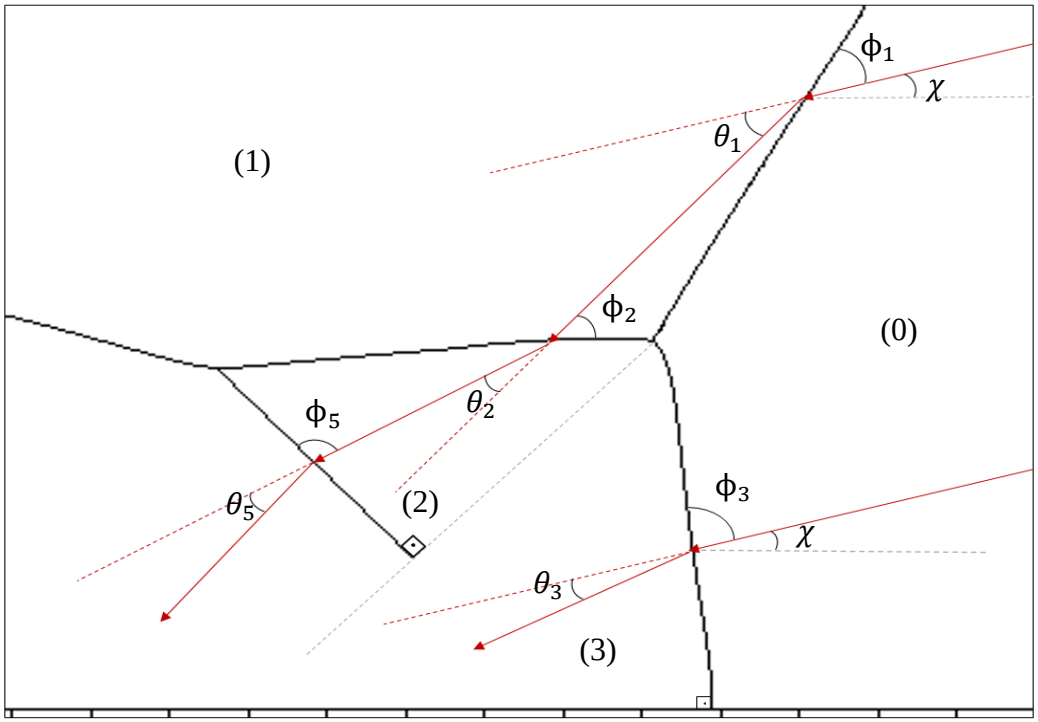


Figure 5.25 All angles and areas for calculations

Final Equation is:

$$\chi' = 90° - \theta_w - \left(tan\left(\frac{\left(1 - \frac{\rho_0}{\rho_1}\right)}{cot(\phi_1) - \left(\frac{\rho_0}{\rho_1}\right) * cot(\phi_2 - \phi_1 - \theta_1)} \right) \right)^{-1}$$

Equation (4.8) is taken from [3].

Unknowns are : ρ_1 , ϕ_1 , ϕ_2 , θ_1

For ρ_1, from Section 4.2:

$$\chi' = 90° - 30° - \left(tan\left(\frac{\left(1 - \frac{1}{\rho_1}\right)}{cot(\phi_1) - \left(\frac{1}{\rho_1}\right) * cot(\phi_2 - \phi_1 - \theta_1)} \right) \right)^{-1}$$

$$\boldsymbol{\rho_1} = \frac{\left((\nu + 1) * {M_s}^2\right)}{(\nu - 1) * {M_s}^2 + 2} * \rho_r = \mathbf{8} \qquad (5.4)$$

For ϕ_1, θ_1:

$$\chi' = 90° - 30° - \left(tan\left(\frac{\left(1 - \frac{1}{8}\right)}{cot(\phi_1) - \left(\frac{1}{8}\right) * cot(\phi_2 - \phi_1 - \theta_1)} \right) \right)^{-1}$$

For finding θ_1, Equation Ben-Dor SWRP (1.3.2.) should be used. But for solving that equation, ϕ_1 should be known.

$$1.4 * tan\phi_1 = \ 8 * tan(\phi_1 - \ \theta_1) \tag{5.5}$$

Otherwise Equation (4.1) and (4.2) could be used but under these conditions, Equation (4.3) and (4.4) should be used.

$$\phi_1 = \frac{\pi}{2} - \ \theta_w - \ \chi$$

For finding ϕ_1, first triple point angle χ should be known because of strong wave effect as mentioned in Section 4.2.

Under these conditions, it is clear that ϕ_1 should be known somehow. As Ben-Dor [9] claimed before, some numerical results are necessary for solving three-shock theory equations. For this reason, the values, which are measured and given in Figure 5.26 approximately from sample simulation 800x200 grid cells at 0.25 end time for 0th DG degree, are;

$\boldsymbol{\rho_2 = 11.5,\ p_2 = 210,\ \chi = 10°,\ \chi' = 11°}$

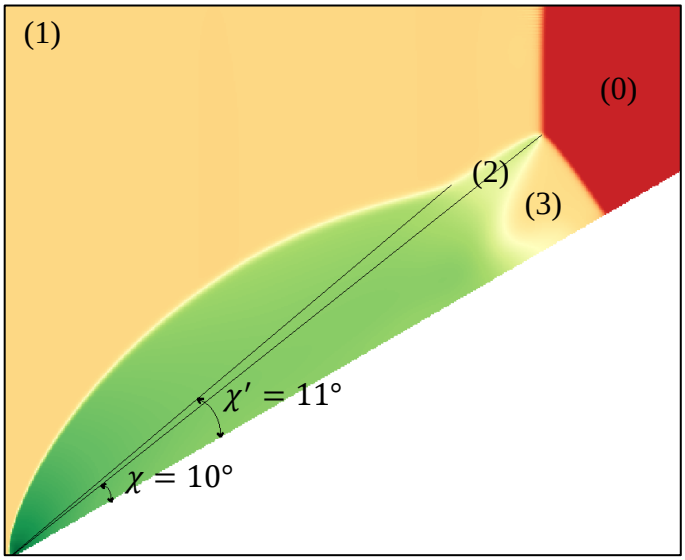


Figure 5.26 Areas and angles on IBM simulation

For $\chi = 10°$, $\boldsymbol{\phi_1 = 50°}$.

$$\boldsymbol{u_0} = \frac{V_s}{\sin(\phi_1)} = \mathbf{13.054} \tag{5.6}$$

$$\boldsymbol{M_0} = \frac{M_s}{\sin(\phi_1)} = \mathbf{13.054} \tag{5.7}$$

For θ_1 Equation (3.23) is used:

$$\chi' = 90° - 30° - \left(tan\left(\frac{\left(1 - \frac{1}{8}\right)}{cot(50°) - \left(\frac{1}{8}\right) * cot(\phi_2 - 50° - \theta_1)} \right) \right)^{-1}$$

$$1.4 * tan(\phi_1) = \rho_1 * tan(\phi_1 - \theta_1) \tag{5.8}$$

$$\boldsymbol{\theta_1 = 38.22°}$$

In this case the values of u_1 which will be needed later can be calculated with incident shock wave equations in Section 3.2.2.2, three shock theory.

$$1.4 * 13.054 * sin(50°) = \ 8 * u_1 * sin(50° - \ 38.22°) \tag{5.9}$$

$$\boldsymbol{u_1 = 8.5719}$$

For finding ϕ_2, Section 1.3.2. of reference [9] and Section 3.2.2 of this thesis:

$$\chi' = 90° - 30° - \left(tan\left(\frac{\left(1 - \frac{1}{8}\right)}{cot(50°) - \left(\frac{1}{8}\right) * cot(\phi_2 - 50° - 38.22°)} \right) \right)^{-1}$$

$$8 * 8.5719 * sin\phi_2 = \ 11.5 * u_2 sin(\phi_2 - \ 3°)$$

$$116.5 + \ 8 * 8.5719^2 sin^2\phi_2 = \ 210 + \ 11.5 * u_2^2 sin^2(\phi_2 - \ 3°)$$

$$8 * tan\phi_2 = \ \rho_2 tan(\phi_2 - \ 3°)$$

$$\boldsymbol{\phi_2 = 40.89°}$$

Finally, $\boldsymbol{\chi' = 11°}$ which is measured from simulation 800x200 grid cells at 0.25 end time for 0th DG degree.

While all these processes are performed, some results of the sample simulation had used, so the actual verification takes place in itself. While measuring the values from sample simulation, we observed that all ρ_0, ρ_1, p_0, p_1 values which are calculated before

are the same with sample simulation results. Calculations were not done for each simulation individually as the values are sufficiently close to or identical to each other.

If the values which are obtained are applied to momentum equations for incident shock wave, reflected shock wave and Mach stem:

- Across the incident shock wave, i: $140.99 \approx 141.08$
- Across the reflected shock wave, r: $368.388 \approx 388.328$
- Across the Mach stem, m: $232.37 \approx 225.49$

The errors are calculated with:

$$\frac{x_1 - x_2}{x_2} \tag{5.10}$$

Error of incident shock wave, i: $(141.08 - 140.99)/140.99 = 0.06\%$

Error of reflected shock wave, r: $(388.328 - 368.388)/368.388 = 5.4\%$

Error of Mach stem, m: $(232.37 - 225.49)/225.49 = 3\%$

The highest error is observed for reflected shock wave, r. The possible reason of this can be about limited opportunities about measuring the plots while using VisIt. Another possibility can be about the problems which are observed while performing simulations.

All calculations were made with weak shock wave assumptions previously than strong wave. If weak shock waves would be considered, ϕ_1 could be found easily without numerical aim. In this conditions calculating order would be like below after Equation (5.4).

Continue from the part of finding $\phi_1,\ \theta_1$:

$$\chi' = 90° - 30° - \left(tan\left(\frac{\left(1 - \frac{1}{8}\right)}{cot(\phi_1) - \left(\frac{1}{8}\right) * cot(\phi_2 - \phi_1 - \theta_1)} \right) \right)^{-1}$$

For finding θ_1, Equation (1.3.2.) of [9] should be used.

$1.4 * tan\phi_1 = \ 8 * tan(\phi_1 - \theta_1)$

Due to weak wave assumption: $\boldsymbol{\phi_1} = \frac{\pi}{2} - \ \theta_w = \mathbf{60°}$ and hence $\boldsymbol{\theta_1} = \mathbf{43°}$

$$\boldsymbol{u_0} = \frac{V_s}{\sin(\phi_1)} = \mathbf{11.547} \tag{5.11}$$

$$\boldsymbol{M_0} = \frac{M_s}{\sin(\phi_1)} = \mathbf{11.547} \tag{5.12}$$

In this case the values of u_1 which will be needed later can be calculated with incident shock wave equations in Section 3.2.2.2, three shock theory.

$$1.4 * 11.547 * sin(60°) = \ 8 * u_1 * sin(50° - \ 43°) \tag{5.13}$$

$$\boldsymbol{u_1 = 5.985}$$

When Mach stem is perpendicular to surface: $\boldsymbol{\theta_3 = 0°, \phi_3 = 90°}$ [11].

$$48 * sin\phi_2 = \ \rho_2 * u_2 * sin(\phi_2 - \ 43°) \tag{5.14}$$

$$116.5 + \ 288 * sin^2\phi_2 = \ p_2 + \ \rho_2 * u_2^2 * sin^2(\phi_2 - \ 43°) \tag{5.15}$$

$$8 * tan\phi_2 = \ \rho_2 * tan(\phi_2 - \ 43°) \tag{5.16}$$

Numerical results are not used until here for calculations of weak wave. Numerical results which are necessary: $\boldsymbol{\rho_2 = 11.5,\ p_2 = 210}$.

$$4.74 * sin\phi_2 = \ u_2 sin(\phi_2 - \ 43°) \tag{5.17}$$

$$288 * sin^2\phi_2 = \ 93.5 + \ 11.5 * u_2^2 * sin^2(\phi_2 - \ 43°) \tag{5.18}$$

$$0.7 * tan\phi_2 = \ tan(\phi_2 - \ 43°) \tag{5.19}$$

With one unknown:

$$\begin{aligned} 0 = 93.3 + 11.5 * & \left(\frac{5 * sin(\phi_2)}{sin(\phi_2 - 43)}\right)^2 \\ & * \left(sin\left(arctan\left(0.6956521739 * tan(\phi_2)\right)\right)\right)^2 - 412 \\ & * sin^2(\phi_2) \end{aligned} \tag{5.20}$$

Equation (5.20) could be solved by neither Maple nor Matlab.

Calculations for weak waves, less numerical results are needed than strong wave because of ϕ_1 which is associated with first triple point χ for strong waves.

CHAPTER 6

RESULTS AND DISCUSSION

Obtained results, which were observed during thesis, are listed below.

- The mentioned kink is not observed in the simulations with higher DG degrees or IBM simulations.
- Higher DG degree solutions are more affecting to have better results than higher grid cell solutions.
- First or second triple point angles cannot be calculated without numerical results.
- The ρ and p values, which are obtained from all the simulations which are performed, are the same with each other at most 0.3% difference.
- Using different Y values for simulations does not affect the results.
- Simulations, which are performed, are similar to reference article [1].
- It is understood that the locations of the triple points of DMR cannot be determined without numerical studies and many assumptions.
- The final calculations for observing error was done successfully. The maximum error was for reflected shock wave r, 5.4%.

Obtained proposals, which occurred during thesis, are listed below.

- Immersed boundary method still needs to be understood better for performing the simulations with high quality. The expected quality results could not be obtained by the solution codes.
- As a result of the investigations in Section 5.4.2, in Double Mach reflection solutions, area (3) needs to be investigated more.

- The Kink on Mach Stem from simulations for 0^{th} DG degree has to be investigated. This problem can be about less sensitive solution caused by lowest DG degree level.
- The equations for triple points of DMR need to be developed for verifying without numerical studies.
- Errors, especially for reflected shock wave, should be reduced.
- Another method can be found for measuring the simulations plots better from VisIt.
- Another method can be found for defining the figures' points better as picture from Engauge Digitizer.

REFERENCES

[1] Lui, C. and Hu, C., (2017). "An Immersed Boundary Solver for Inviscid Compressible Flows", Research Institute for Applied Mechanics, Kyushu University, 2017;1–22, Fukuoka.

[2] Anderson, J.D., (1990). "Modern Compressible Flow with Historical Perspective", Third Edition, Mc Graw-Hill, New York.

[3] Ben-Dor, G. (1980). "Analytical Solution of Double-Mach Reflection", 18:80–4088, Beer Sheva.

[4] Müller, B., (2014). "Methods for Higher Order Numerical Simulations of Complex Inviscid Fluids with Immersed Boundaries", PhD thesis, Technical University of Darmstadt Chair of Fluid Dynamics, Darmstadt.

[5] Müller, B., Kummer, F., et al. (2016). "A High-order Discontinuous Galerkin Method for Compressible Flows with Immersed Boundaries", International Journal of Numerical Methods in Engineering, 295:475–504, Darmstadt.

[7] Müller, B., Kummer, F., et al. (2017). "The BoSSS Handbook", Technical University of Darmstadt, Darmstadt.

[8] Anderson, J.D., (1991). "Fundamentals of Aerodynamics", Second Edition, Mc Graw-Hill, New York.

[9] Ben-Dor, G. (2007). "Shock Wave Reflection Phenomena", Second Edition, Springer, Heidelberg.

[10] Law, C.K. (1970). "Diffraction of Strong Shock-Waves by Sharp Compressive Corner", Utias, Toronto.

[11] Ben-Dor, G., Li, H., Chpoun, A. and Passerel D. (1995). "Reconsideration of Oblique Shock Wave Reflections in Steady Flows. Part 1. Experimental Investigation", 301:19–35, 19 May 1995, Beer Sheva.

[12] Ben-Dor, G. and Li, H. (1994). "Reconsideration of Pseudo-steady Shock Wave Reflections and the Transition Criteria Between Them", Ben-Gufion University of the Negev, 5:59–73, 10 November 1994, Beer Sheva.

APPENDIX-A

COMPRESSIBLE NAVIER-STOKES SOLVER

The codes which are used for Compressible Navier-Stokes Solver (CNS) are shown in this chapter. Figures A.1, A.2, A.3, A.4, A.5 and A.6 belong to a file which is used for performing simulation 800x200 grid cells at 0.20 end time for 3rd DG degree. Most of the codes are given by the supervisor and are not an onus for the thesis. The lines which are changed for performing simulations are explained in details.

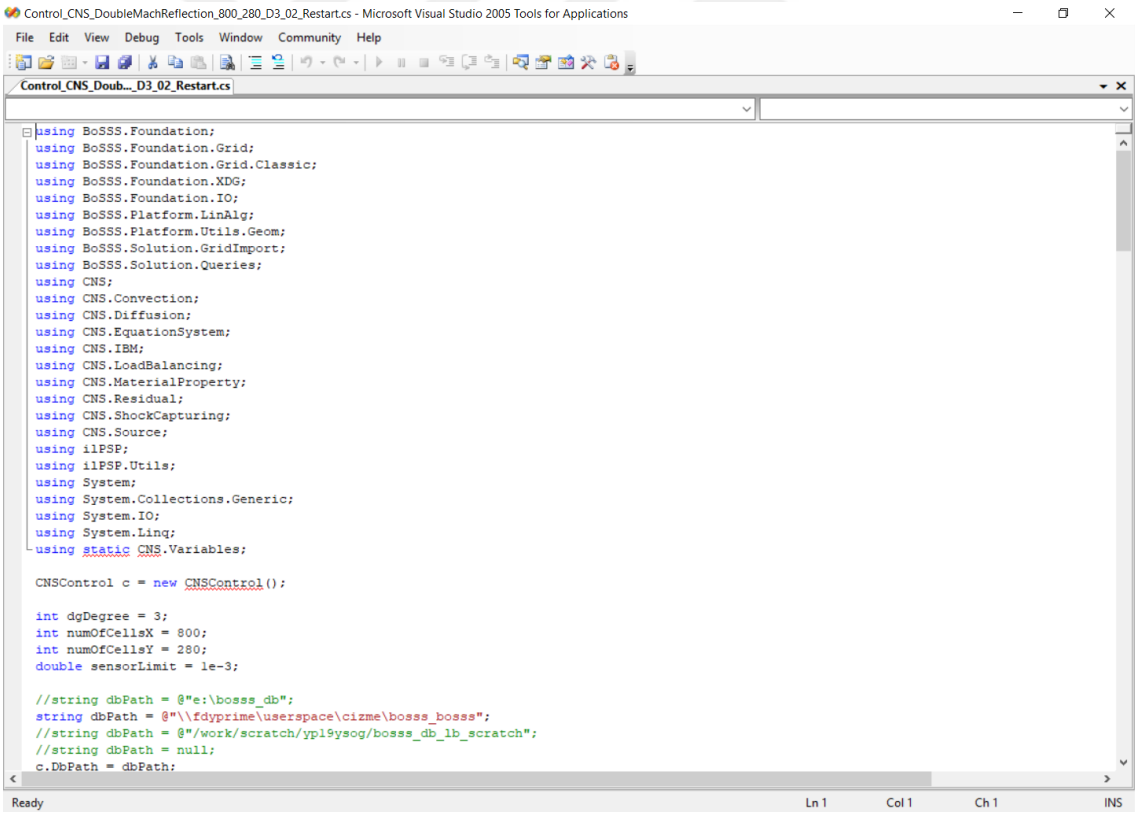


Figure A.1 First part of the CNS file of the simulation 800x200 grid cells at 0.20 end time for 3rd DG degree

The line “using CNS.IBM”, which is seen in Figure A.1, is added to CNS files for IBM simulations. The line “using CNS.LoadBalancing” is used for the simulations for 1st, 2nd and 3rd DG degrees.

Also the lines which are starting with “int” can be seen in Figure A.1. The line “int dgDegree = 3” shows that the simulation will perform for 3rd DG degree, the line “int numOfCellsX = 800” shows that the simulations has 800 grid cells in x-direction and the line “int numOfCellsY = 280” shows that the simulation has 280 grid cells in y-direction.

The line “double sensorLimit = 1e-3” is necessary for performing Double Mach Reflection simulations and about smoothness of jumpings during property changings.

The green lines which are seen in Figure A.1 and also Figure A.2, A.3, A.4, A.5 and A.6 have “//” sign in the beginning of the line and that sign makes that line not active.

The lines starting with “string dbPath” show the folder which is used for saving data after solving the respective CNS file.

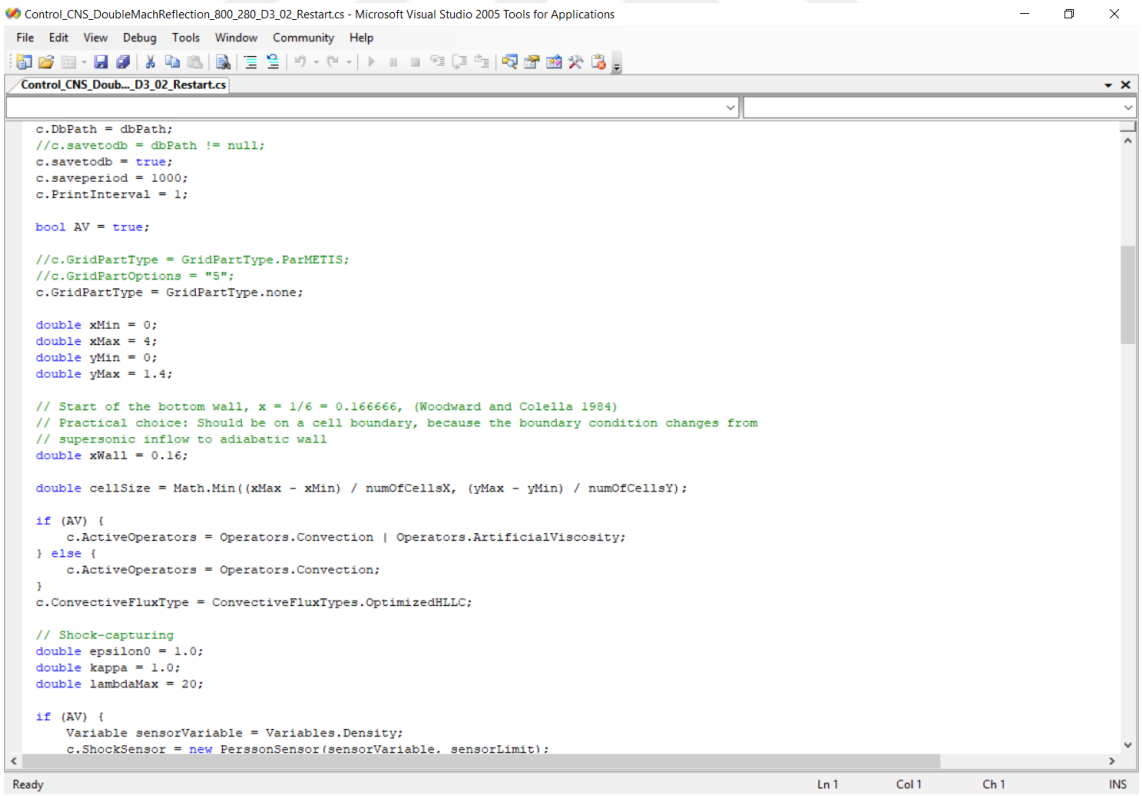


Figure A.2 Second part of the CNS file of the simulation 800x200 grid cells at 0.20 end time for 3rd DG degree

The line “c.saveperiod = 1000”, which is seen in Figure A.2, shows that the saving data period is 1000. The lines “double xMin = 0”, “double xMax = 4”, “double yMin = 0” and “double yMax = 1.4” show that the minimized versions of grid cells.

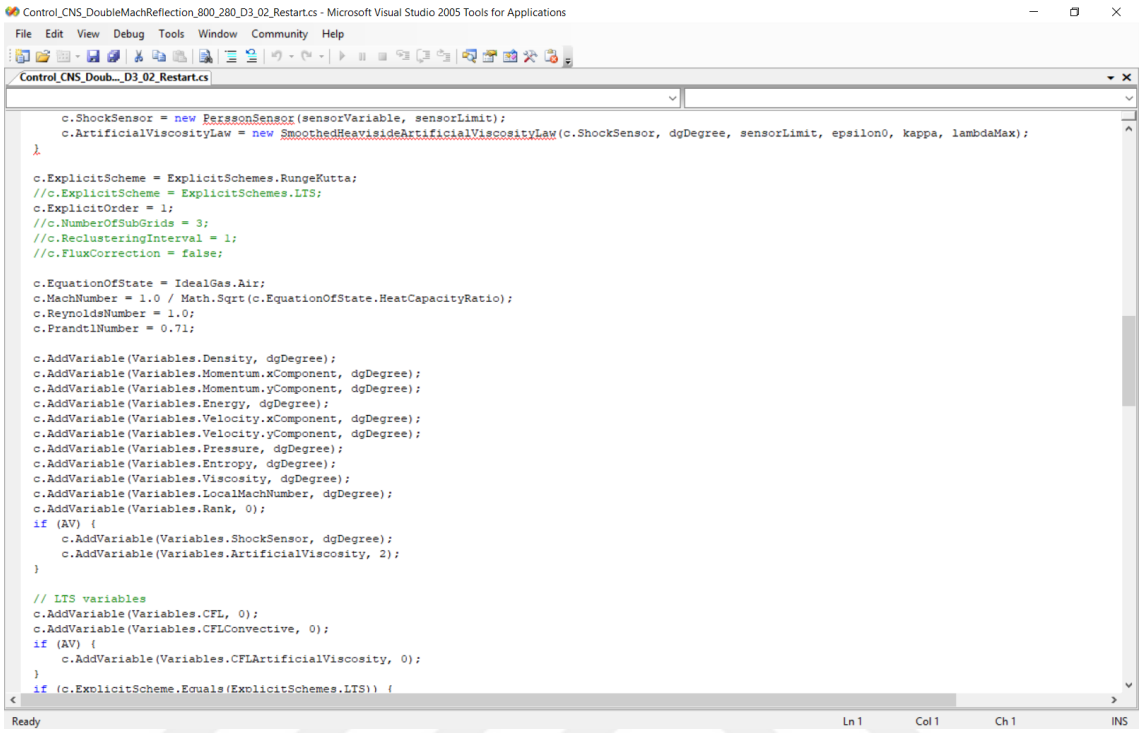


Figure A.3 Third part of the CNS file of the simulation 800x200 grid cells at 0.20 end time for 3rd DG degree

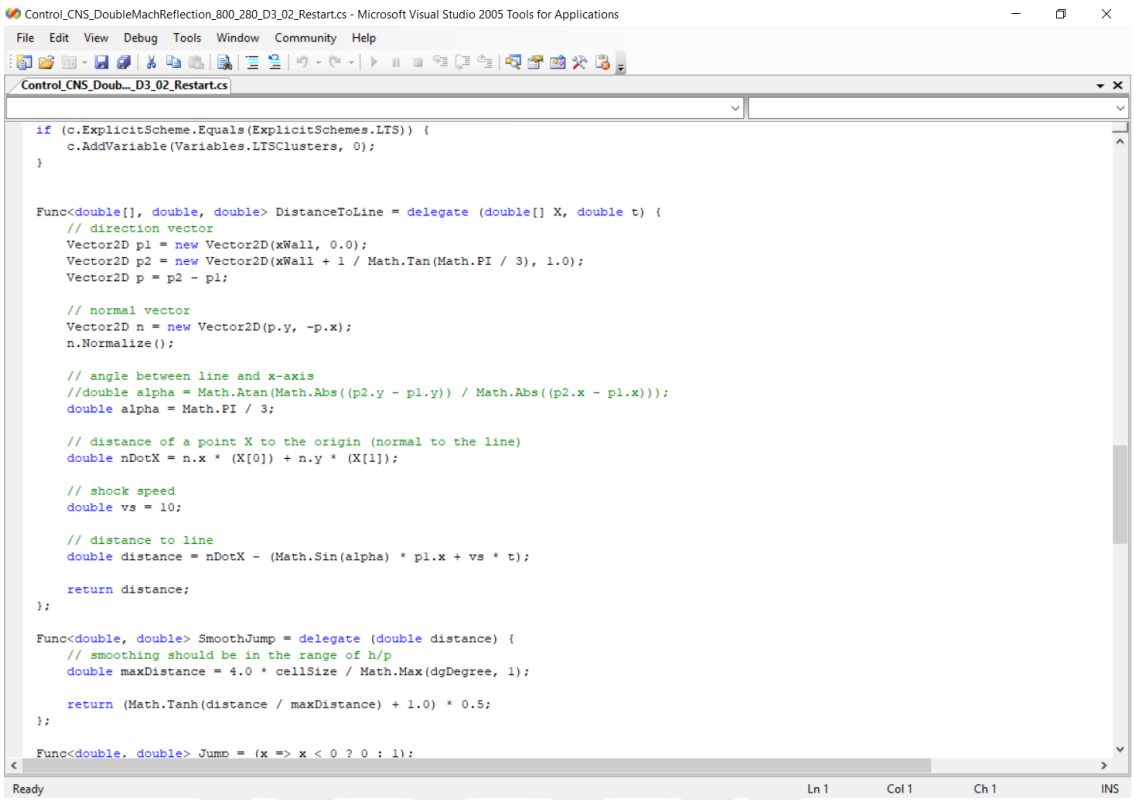


Figure A.4 Fourth part of the CNS file of the simulation 800x200 grid cells at 0.20 end time for 3rd DG degree

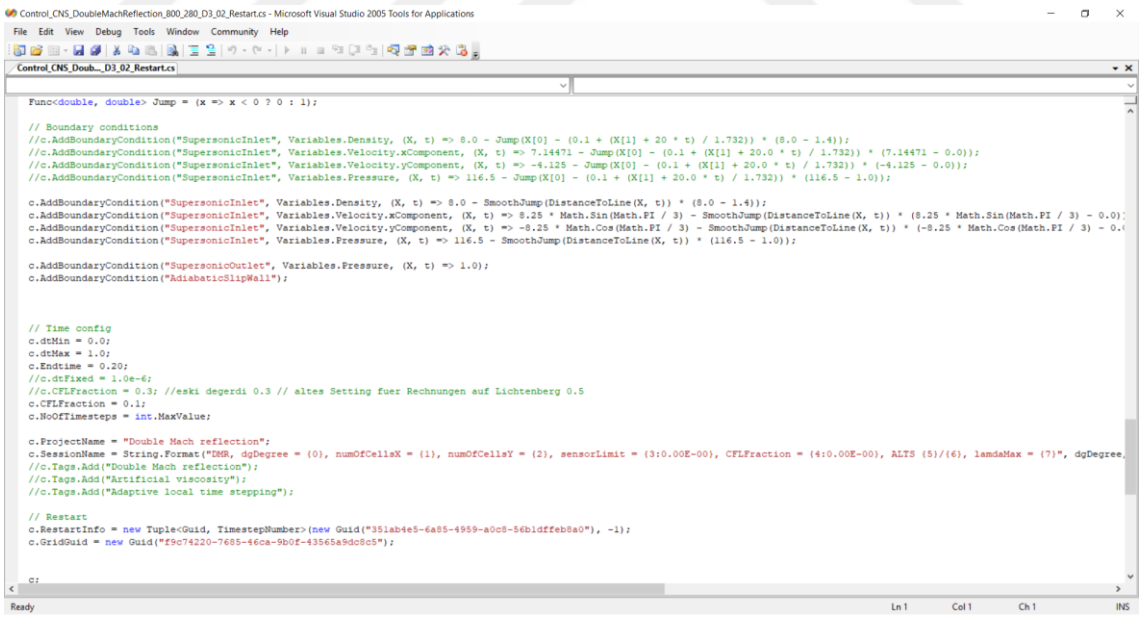


Figure A.5 Fifth part of the CNS file of the simulation 800x200 grid cells at 0.20 end time for 3rd DG degree

In Figure A.5, boundary conditions can be seen. The simulations for 1st, 2nd and 3rd DG degrees should use smooth jump because of defining the sudden changings of properties.

The part starting with "// Restart" is used for continuing to performing simulations. With any reason (electricity, technical problems, code problems etc.), HPC can stop performing simulations. For these situations "c.RestartInfo = " and "c.GridGuid = " lines should be added to CNS file before using HPC again. The reason of this is, every simulation has its own session and grid number which define the respective simulation. For continuing the same simulation is only possible with adding the new data to old one.

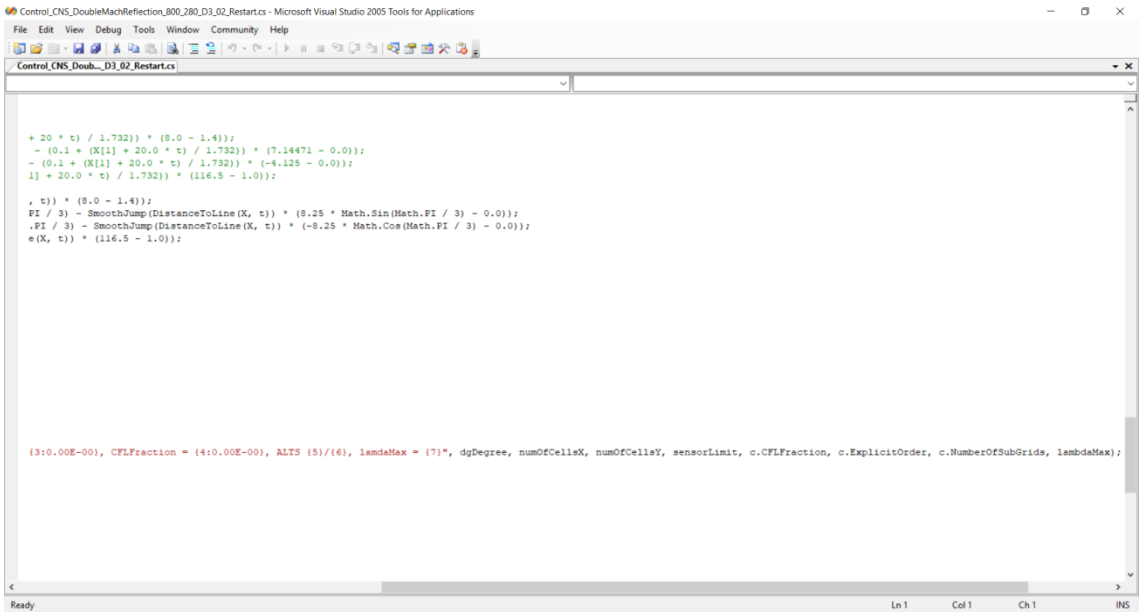


Figure A.6 Continuation of Figure A.5

.

CURRICULUM VITAE

PERSONAL INFORMATION

Name Surname : Burcu ÇİZME

Date of birth and place : 07.07.1993, Isparta

Foreign Languages : English, German

E-mail : burcucizme@gmail.com

EDUCATION

Degree	Department	University	Date of Graduation
Undergraduate	Mechanical Engineering	Akdeniz University	06.2015
High School	Science and Mathmatics	Gazi Anatolian High School	06.2011

WORK EXPERIENCE

Year	Corporation/Institute	Enrollment
2017-2018	Ada Makine	08.2017
2015-2017	Vemeks Engineering	09.2015

PUBLISHMENTS

Conference Papers

1. Çizme, B. (2018). "Numerical Study of the Double Mach Reflection Using Shock-capturing with Sub-cell Accuracy", 4th International Conference on Advances in Mechanical Engineering, 19-21 December 2018, İstanbul.